

## MOLECULAR GAS AND STAR FORMATION IN THE NUCLEUS OF IC 342: C<sup>18</sup>O AND MILLIMETER CONTINUUM IMAGING

DAVID S. MEIER AND JEAN L. TURNER

Department of Physics and Astronomy, University of California, Los Angeles, CA 90095-1562; meierd@astro.ucla.edu, turner@astro.ucla.edu  
Received 2000 October 28; accepted 2000 December 14

### ABSTRACT

We present high-resolution maps ( $\sim 2''$ ) maps of the  $J = 1-0$  and  $J = 2-1$  transitions of C<sup>18</sup>O in the central  $\sim 150$  pc of the gas-rich nucleus, IC 342, made with the Owens Valley Millimeter Array. From the C<sup>18</sup>O maps, we are able to obtain the most accurate map of  $N_{\text{H}_2}$  to date for IC 342. Because of their low opacities, the transitions of C<sup>18</sup>O give a more reliable estimate of the true molecular gas column-density distribution than the more common <sup>12</sup>CO and <sup>13</sup>CO isotopomers. The morphology of the C<sup>18</sup>O emission in the nucleus is a minispiral similar to that of the main isotopomer, <sup>12</sup>CO, except that it is more symmetric and lacks the enhancements to the north. We suggest that the asymmetries present in <sup>12</sup>CO images may reflect the viewing perspective of the starburst region biased by the high optical depths of <sup>12</sup>CO rather than true asymmetries in the amount of molecular gas present. The giant molecular clouds seen in C<sup>18</sup>O appear to be nonspherical, probably because of tidal arm shearing. Column densities determined from C<sup>18</sup>O observations, 1.3 mm dust continuum, and the virial theorem indicate that the standard Galactic conversion factor,  $X_{\text{CO}}$ , overestimates the amount of molecular gas in the center of IC 342 by a factor of  $\sim 2-3$  at the molecular cloud peaks and by more than this in the diffuse gas away from the starburst. Revised molecular masses based on this conversion factor imply that star formation efficiencies in the starburst region are very high. From the distribution of gas and star formation, it appears that the sites of star formation are dynamically determined rather than driven by density peaks. Near the central star-forming region, evidence is seen for chemical enrichment of C<sup>18</sup>O caused by massive stars.

*Subject headings:* galaxies: individual (IC 342) — galaxies: nuclei — galaxies: starburst —  
radio lines: galaxies

### 1. INTRODUCTION

Our current knowledge about molecular gas in galaxies is based primarily on the bright, optically thick lines of <sup>12</sup>CO, using the Galactic standard conversion factor  $X_{\text{CO}}$ . These assumptions, while probably adequate when applied to the disks of large spiral galaxies such as our own (Solomon et al. 1987; Scoville & Sanders 1987; Wilson & Scoville 1990; Nakai & Kuno 1995), may not apply in the unusual conditions present in nuclear starbursts. Enhanced metallicities, densities and temperatures, large turbulent line widths, and intense radiation fields that are present in galactic centers may change the value of  $X_{\text{CO}}$  (e.g., Maloney & Black 1988; Elmegreen 1989; Sakamoto 1996). It has been suggested that the  $X_{\text{CO}}$  overestimates gas masses in our own Galactic center by factors of 5–16 (Sodroski et al. 1994; Dahmen et al. 1998) and in nearby starbursts (e.g., Smith et al. 1991; Xie, Young, & Schloeb 1994; Mauersberger et al. 1996; Braine et al. 1997).

Optically thin lines are promising probes of the molecular gas because they are able to “sample” all the column density and not just conditions at cloud edges. Unfortunately, because the abundances of the isotopic species are much lower, the emission lines are relatively weak. Only recently has instrumentation reached the point where interferometric studies of isotopomers in other galaxies are feasible. High-resolution studies of <sup>13</sup>CO (e.g., Hurt & Turner 1991; Turner & Hurt 1992, hereafter TH92; Papadopoulos, Seaquist, & Scoville 1996; Aalto et al. 1997; Neininger et al. 1998; Matsushita et al. 1998; Reynaud & Downes 1999; Meier, Turner, & Hurt 2000, hereafter MTH00) indicate that even <sup>13</sup>CO is optically thick in the massive clouds of

starburst nuclei (Wall & Jaffe 1990; Papadopoulos et al. 1996; MTH00). Therefore, C<sup>18</sup>O may be the best hope for determining true molecular gas distributions of nuclear starburst regions.

IC 342 provides an excellent galaxy for studying the relative locations of different molecular gas tracers within the nuclei of galaxies because it is the closest large spiral with active nuclear star formation (1.8 Mpc, Table 1; McCall 1989; Madore & Freedman 1992; Karachentsev & Tikhonov 1993; see Buta & McCall 1999 for a detailed discussion of the distance to IC 342). IC 342 is nearly face-on, with widespread resolvable molecular line emission both in dense clouds and a diffuse medium (e.g., Lo et al. 1984; Ishizuki et al. 1990; Downes et al. 1992; Wright et al. 1993).

In this paper, the true distribution of the molecular gas in the nucleus of IC 342 will be investigated in order to address questions such as what is the distribution of H<sub>2</sub>? What is  $X_{\text{CO}}$ ? Does  $X_{\text{CO}}$  vary over the starburst region? and Does it correlate with the observed physical conditions of the molecular gas? With these goals in mind, we obtained  $\sim 2''$  resolution Owens Valley Millimeter Interferometer images of C<sup>18</sup>O(2–1), C<sup>18</sup>(1–0), 2.6 and 1.3 mm continuum of the central region of IC 342, giving spatial resolutions of  $\sim 15-20$  pc. The C<sup>18</sup>O(2–1) was observed simultaneously with C<sup>18</sup>O(1–0) to allow determination of  $T_{\text{ex}}$ , which is necessary for the determination of optically thin column densities. These observations are combined with previous data of the  $J = 2-1$  and  $1-0$  transitions of <sup>12</sup>CO and <sup>13</sup>CO (TH92; Turner, Hurt, & Hudson 1993; MTH00) to obtain a detailed and accurate description of the molecular gas column density within the central 150 pc.

TABLE 1  
IC 342 BASIC DATA

| Characteristic                               | Value                               | Reference |
|--|-------------------------------------|-----------|
| Revised Hubble class .....                   | Sab(rs)cd                           | 1         |
| Dynamical center (J2000).....                | 03 46 48.7 ± 0.3<br>+68 05 46.8 ± 2 | 2         |
| 2 μm peak (J2000).....                       | 03 46 48.3 ± 0.3<br>+68 05 46.8 ± 2 | 3         |
| $l^{\text{II}}, b^{\text{II}}$ (deg) .....   | 138.2, +10.6                        | 1         |
| $V_{\text{LSR}}$ (km s <sup>-1</sup> ) ..... | 35                                  | 2         |
| Adopted distance (Mpc) .....                 | 1.8                                 | 4         |
| Inclination (deg) .....                      | 30                                  | 5         |
| Position angle (deg) .....                   | 39.4                                | 5         |
| $B_T$ (mag).....                             | 9.16                                | 1         |

NOTE.—Units of right ascension are hours, minutes and seconds, and units of declination are degrees, arcminutes, and arcseconds.

REFERENCES.—(1) de Vaucouleurs, de Vaucouleurs, & Corwin 1976; (2) TH92; (3) Becklin et al. 1980; (4) McCall 1989; (5) Crosthwaite, Turner, & Ho 2000.

## 2. OBSERVATIONS

Aperture synthesis observations of both C<sup>18</sup>O(1–0) (109.782 GHz) and C<sup>18</sup>O(2–1) (219.560 GHz) were made with the Owens Valley Radio Observatory (OVRO) Millimeter Interferometer between 1997 October 22 and 1997 December 15 (Table 2). The interferometer consists of six 10.4 m antennas with cryogenically cooled SIS receivers (Padin et al. 1991; Scoville et al. 1994). System temperatures (single sideband) ranged from 250 to 400 K at 2.6 mm and 450–1000 K at 1.3 mm.

The transitions were observed simultaneously making use of OVRO's multiple-line spectrometer capabilities. Therefore, both transitions have consistent instrumental configurations, phase centers, and weather. The (2–1) data have the same ( $u, v$ )-pattern but with twice the scale as the (1–0) data. A filter bank with 32 4 MHz channels was used, giving velocity resolutions (bandwidths) of 10.9 km s<sup>-1</sup> (349 km s<sup>-1</sup>) at 2.6 mm and 5.5 km s<sup>-1</sup> (175 km s<sup>-1</sup>) at 1 mm. The systemic velocity of IC 342 with respect to LSR is 35 km s<sup>-1</sup> and was centered at channel 16.5. Two pointings with phase centers of  $\alpha_1(\text{B1950}) = 03^{\text{h}}41^{\text{m}}57^{\text{s}}.9$ ,  $\delta_1(\text{B1950}) = +67^{\circ}56'29''.0$  and  $\alpha_2(\text{B1950}) = 03^{\text{h}}41^{\text{m}}57^{\text{s}}.0$ ,  $\delta_2(\text{B1950}) = +67^{\circ}56'26''.0$  were observed to cover the entire nuclear minispiral. Data were calibrated using the MMA software package. Calibrators 3C 84 and 0224+671 were observed in 20 minute intervals for phase calibration. Absolute flux calibration was done using Neptune and Uranus as primary flux calibrators and 3C 273 as a secondary flux calibrator for both transitions. Absolute flux calibrations are esti-

mated to be good to 10%–15% for the 2.6 mm data and 20%–25% for the 1.3 mm data.

The data set was mosaiced using the MIRIAD package. The maps are naturally weighted and primary-beam corrected. Since the maps are mosaics, noise levels vary across the maps. Noise levels reported throughout this paper are those measured from line-free channels of the spectral cube half-way between the map center and the FWHM points. The true noise level is slightly lower (~10%) at the phase centers and somewhat higher toward the edge of the primary beams. All further data reduction was done with the NRAO AIPS package. In making the zeroth moment (integrated intensity) maps, only emission greater than 1.2  $\sigma$  was included. Because the signal-to-noise ratio (S/N) is lower in the C<sup>18</sup>O(2–1) map, the choice of 1.2  $\sigma$  could, in principle, lower the integrated intensities of the C<sup>18</sup>O(2–1) map relative to the higher sensitivity C<sup>18</sup>O(1–0) map. However, the ratio of the integrated intensity maps made with no clipping is identical to those with clipping to within 5%, indicating this effect is not important.

The ( $u, v$ )-coverage for these observations implies that emission on scales larger than ~36'' (3 mm) or ~18'' (1.3 mm) is resolved out. To estimate the amount of extended flux the interferometer resolves out in the C<sup>18</sup>O(1–0) map, it was compared with the single-dish spectra from the 30 m IRAM telescope (Eckart et al. 1990) at 21'' resolution. The integrated intensity of the OVRO map when convolved to 21'' is 3.6 K km s<sup>-1</sup>, which is ~67% of the 4.8 K km s<sup>-1</sup> detected by IRAM. This is consistent with the 70%–75% detected in the <sup>12</sup>CO(1–0) map (Levine et al. 1994) and not much lower than the 80% estimated for the <sup>13</sup>CO transitions (TH92; MTH00). A similar analysis yields 4.9 K km s<sup>-1</sup> for C<sup>18</sup>O(2–1) or ~60% of the single-dish flux. Therefore, the amounts of flux resolved out in <sup>12</sup>CO(1–0), <sup>13</sup>CO, and C<sup>18</sup>O are all similar and should not strongly effect the intercomparisons.

## 3. RESULTS

### 3.1. The C<sup>18</sup>O Morphology

The C<sup>18</sup>O(1–0) and C<sup>18</sup>O(2–1) channel maps are presented in Figures 1 and 2. Peak antenna temperatures obtained in the 4 MHz channels are ~0.75 K for C<sup>18</sup>O(1–0) and 1.5 K for C<sup>18</sup>O(2–1). Emission is present in channels from  $V_{\text{LSR}} = -14$  km s<sup>-1</sup> to 73 km s<sup>-1</sup> with higher velocities in the northeast. The line center and velocity dispersions of both transitions of C<sup>18</sup>O are consistent with those of <sup>13</sup>CO (TH92). Integrated intensity maps of the C<sup>18</sup>O(1–0) and C<sup>18</sup>O(2–1) transitions, along with the <sup>12</sup>CO(1–0) map (Levine et al. 1994) are plotted to the same scale in Figure 3. Integrated intensities of each transition are listed in Table 3

TABLE 2  
OBSERVATIONAL DATA<sup>a</sup>

| Transition <sup>b</sup>      | Frequency (GHz) | $T_{\text{ssb}}$ (K) | $\Delta V_{\text{chan}}$ (km s <sup>-1</sup> ) | $\Delta v_{\text{band}}$ (MHz) | Beam Size (arcsec; deg) | Noise Level (K/mJy beam <sup>-1</sup> ) |
|------------------------------|-----------------|----------------------|--|--------------------------------|-------------------------|---|
| C <sup>18</sup> O(1–0) ..... | 109.782         | 400–450              | 10.92  | 128                            | 3.3 × 3.0; –43°         | 0.062/6                                 |
| C <sup>18</sup> O(2–1).....  | 219.560         | 430–1050             | 5.46   | 128                            | 1.8 × 1.6; –26°         | 0.14/16                                 |
| 3 mm continuum.....          | 109.5           | 360–430              | ...  | 1000                           | 3.3 × 3.0; –44°         | 0.004/0.40                              |
| 1 mm continuum.....          | 219.8           | 400–1000             | ...  | 1000                           | 1.9 × 1.6; –15°         | 0.016/2                                 |

<sup>a</sup> For observations made from 1997 Oct 22 to 1997 Dec 12.

<sup>b</sup> Phase Center 1:  $V_{\text{LSR}} = 35$  km s<sup>-1</sup>;  $\alpha = 03^{\text{h}}46^{\text{m}}48^{\text{s}}.10$ ,  $\delta = +68^{\circ}05'44''.8$  (J2000). Phase Center 2:  $\alpha = 03^{\text{h}}46^{\text{m}}49^{\text{s}}.01$ ,  $\delta = +68^{\circ}05'47''.8$  (J2000).

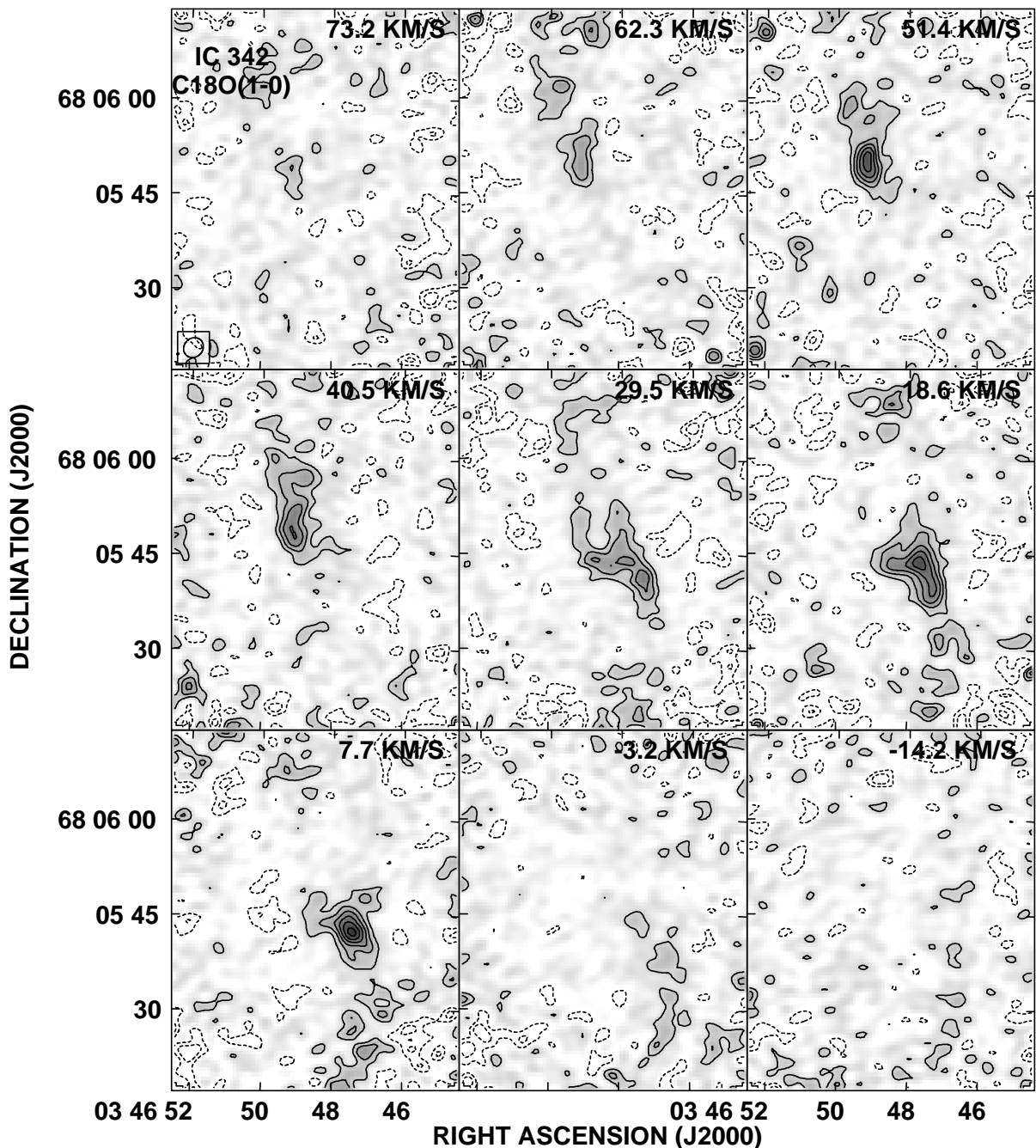


FIG. 1.— $C^{18}O(1-0)$  channel map. LSR velocities are listed at the top right of each plane. Contours are plotted in intervals of  $12 \text{ mJy beam}^{-1}$  (or  $0.12 \text{ K}$  for the  $3''.3 \times 3''.0$  beam) corresponding to  $2\sigma$ . The beam is plotted in the bottom left of the first plane.

for various locations across the nucleus (nomenclature from Downes et al. 1992, Fig. 2 of MTH00).

The basic morphology of the nuclear minispiral seen in  $C^{18}O(1-0)$  is similar to the  $^{12}CO(1-0)$  transition, but there are noticeable differences. Observations of  $^{12}CO$  and HCN show that there are five major peaks of molecular gas in the nucleus (Ishizuki et al. 1990; Downes et al. 1992). GMC C, along the northern arm, is brightest in  $^{12}CO$ , GMC B is the molecular cloud associated with the starburst, and GMC A is nearest to the dynamical center of IC 342. GMCs D and E are the more distant giant molecular clouds along the northern and southern arms, respectively. All GMCs except GMC A are readily seen in  $C^{18}O(1-0)$ . GMC A is substantially weaker in the  $1-0$  transition of  $C^{18}O$  relative to the

$^{12}CO(1-0)$  transition. However, in the  $2-1$  transition of  $C^{18}O$ , GMC A is similar in relative strength. The weakness of GMC A in  $C^{18}O(1-0)$  is probably a temperature effect (§ 3.2.1).

Another difference is that the  $C^{18}O(1-0)$  distribution, like  $^{13}CO(1-0)$  (TH92; Wright et al. 1993), appears more symmetric than  $^{12}CO(1-0)$ . In  $^{12}CO(1-0)$ , the northern arm is brighter than the southern arm by about 50% (the integrated flux of the entire northern arm is  $1200 \text{ Jy km s}^{-1}$ , while the entire southern arm is  $800 \text{ Jy km s}^{-1}$ ). In  $C^{18}O(1-0)$ , it is only  $\sim 15\%$  brighter (the integrated flux of the entire northern arm is  $15.4 \pm 2.5 \text{ Jy km s}^{-1}$ , as compared with  $13.6 \pm 2 \text{ Jy km s}^{-1}$  for the southern arms).  $C^{18}O(1-0)$  preferentially arises from the outside (leading) edges of the

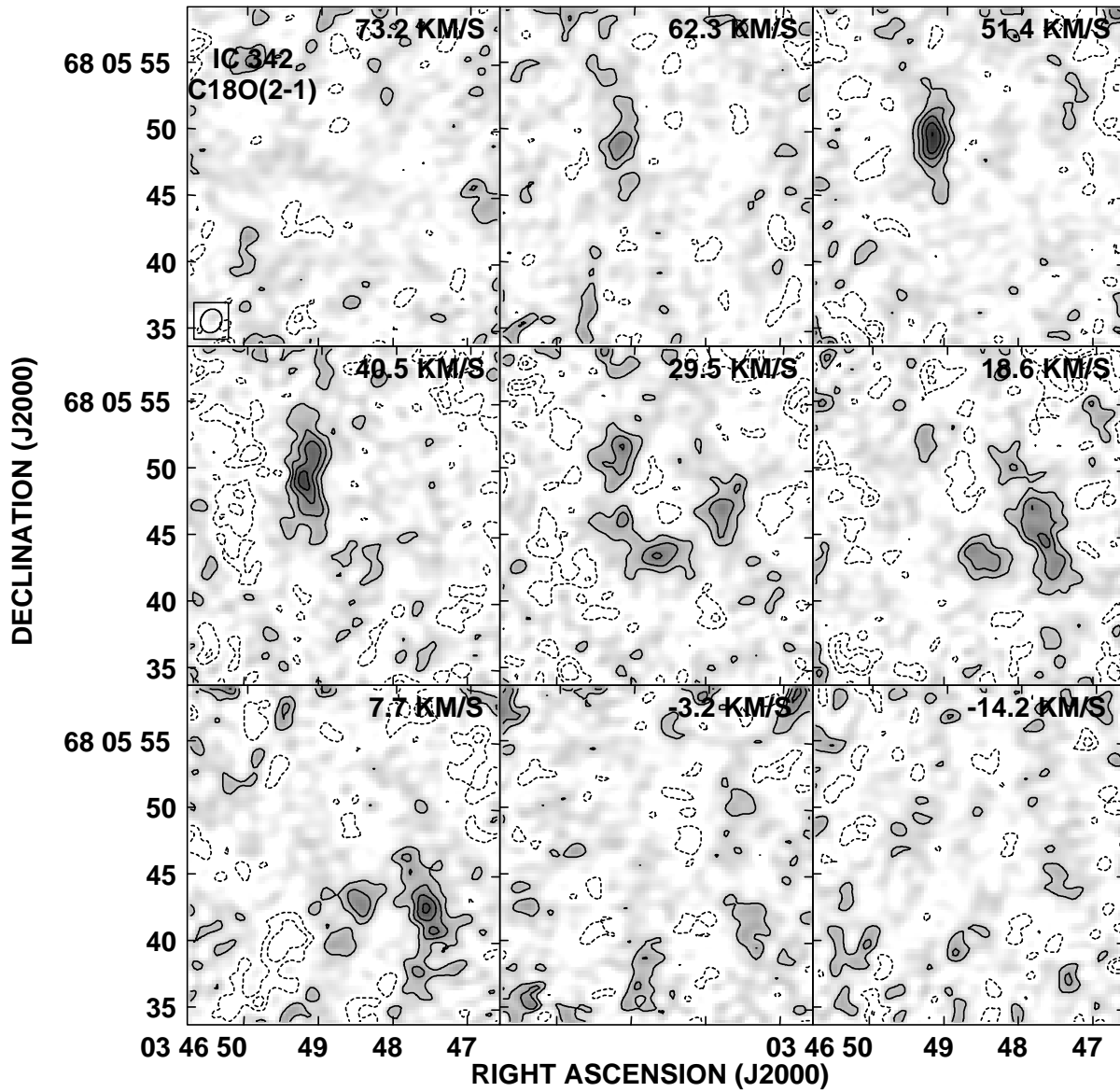


FIG. 2.— $C^{18}O(2-1)$  channel map. LSR velocities listed the same as in Fig. 1. Contours are plotted in intervals of  $32 \text{ mJy beam}^{-1}$  (or  $0.29 \text{ K}$  for the  $1''.8 \times 1''.6$  beam) corresponding to  $2\sigma$ . The beam is plotted in the bottom left of the first plane.

TABLE 3  
MEASURED INTENSITIES AND RATIOS<sup>a</sup>

| Location                          | Position<br>( $3^{\text{h}}46^{\text{m}}, 68^{\circ}05'$ ) | $I(C^{18}(1-0))$<br>( $\text{K km s}^{-1}$ ) | $I(C^{18}(1-0))$<br>( $\text{K km s}^{-1}$ ) | $\frac{C^{18}O(2-1)^{\text{b}}}{C^{18}O(1-0)}$ | $\frac{^{12}CO(1-0)^{\text{b}}}{C^{18}O(1-0)}$ | $\frac{^{13}CO(1-0)^{\text{b}}}{C^{18}O(1-0)}$ |
|-----------------------------------|--|--|--|--|--|--|
| A .....                           | 48.51, 43.4  | $8.7 \pm 1.3$                                | $26 \pm 6.4$                                 | $1.7 \pm 0.50$                                 | $67 \pm 14$                                    | $5.8 \pm 1.2$                                  |
| B .....                           | 47.78, 46.0  | $7.0 \pm 1.3$                                | $25 \pm 6.2$                                 | $2.2 \pm 0.68$                                 | $69 \pm 16$                                    | $7.2 \pm 1.7$                                  |
| C .....                           | 49.19, 49.5  | $22 \pm 3.3$                                 | $43 \pm 10$                                  | $1.2 \pm 0.34$                                 | $32 \pm 7$                                     | $5.4 \pm 1.2$                                  |
| D .....                           | 48.93, 59.2  | $\leq 4.0$                                   | $16 \pm 4$                                   | $\sim 1.0$                                     | $\geq 100$                                     | $\geq 10$                                      |
| E .....                           | 47.50, 42.0  | $21 \pm 3.2$                                 | $26 \pm 6.4$                                 | $0.63 \pm 0.19$                                | $28 \pm 6$                                     | $4.1 \pm 0.90$                                 |
| Arm <sup>c</sup> .....            | 47.10, 33.9  | $4.0 \pm 1.3$                                | ...  | ...  | $\sim 51$                                      | $\sim 4.7$                                     |
| Off-arm <sup>c</sup> .....        | 48.10, $03.8^{\text{d}}$                                   | $\leq 4.0$                                   | ...  | ...  | $\geq 110$                                     | $\geq 7$                                       |
| Central trough <sup>c</sup> ..... | 48.26, 47.8  | $5.3 \pm 1.3$                                | $< 8.0$                                      | ...  | $24 \pm 7$                                     | $3.2 \pm 1.0$                                  |

NOTE.—Units of right ascension are in seconds, and units of declination are in arcseconds.

<sup>a</sup> Measurements of the intensities are based on the resolutions given in Table 2, while the resolutions of the ratio maps are those of the  $C^{18}O(1-0)$  (except the  $^{13}CO(1-0)/C^{18}O(1-0)$  ratio, which has a resolution of  $4''.8 \times 3''.9$ ). The uncertainties reflect the larger of the absolute calibration uncertainty or the map noise.

<sup>b</sup> Ratios are for integrated intensity,  $\int T_b dv$ , rather than the peak intensities.

<sup>c</sup> Positions are taken from MTH00.

<sup>d</sup> Based on  $\alpha = 3^{\text{h}}46^{\text{m}}, \delta = 68^{\circ}06'$ .

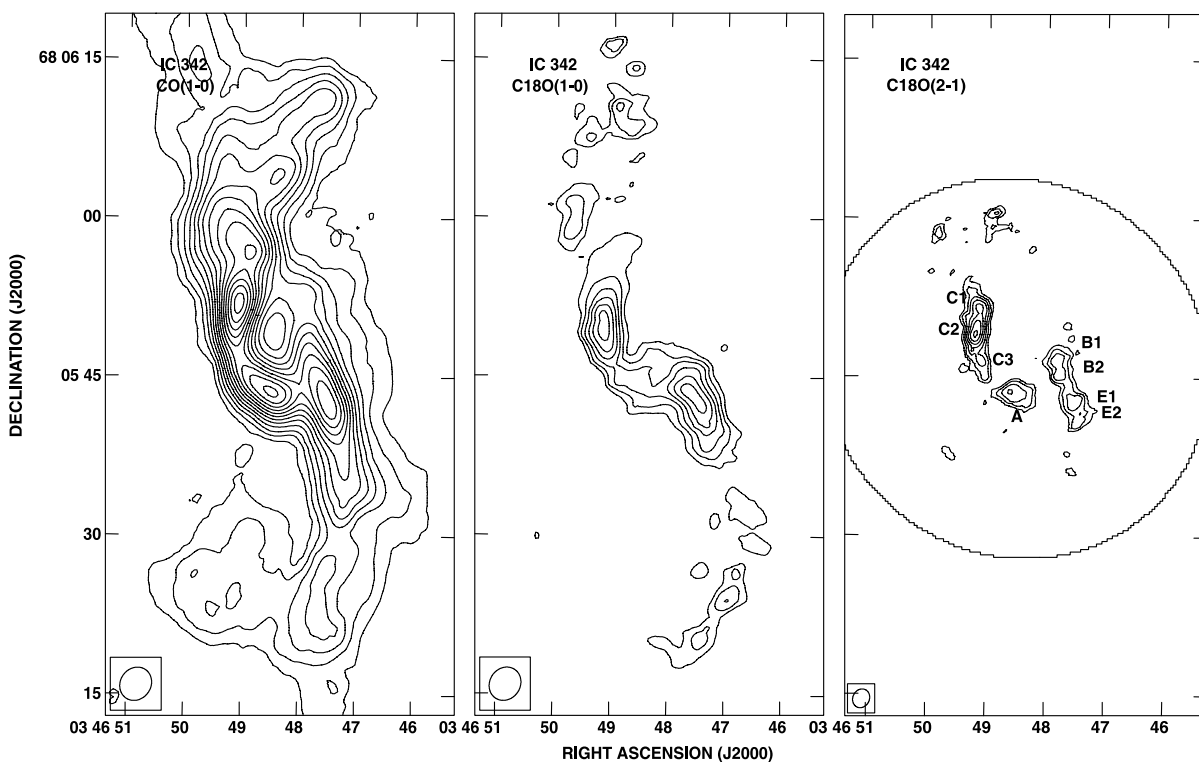


FIG. 3.—Integrated intensity of the transitions. (*Left*)  $^{12}\text{CO}(1-0)$  integrated intensity (Levine et al. 1994). The  $^{12}\text{CO}(1-0)$  map has been convolved to the beam size of the  $\text{C}^{18}\text{O}(1-0)$  map. Contours are in steps of  $47.1 \text{ K km s}^{-1}$ . (*Middle*)  $\text{C}^{18}\text{O}(1-0)$  integrated intensity. Contours are in steps of  $1.32 \text{ K km s}^{-1}$  ( $2\sigma$ ), minus the  $2\sigma$  contour. (*Right*)  $\text{C}^{18}\text{O}(2-1)$  integrated intensity. Contours are the same as in the middle panel with a  $2\sigma$  value of  $2.68 \text{ K km s}^{-1}$ . The large circle marks the FWHM power points of the mosaiced  $(2-1)$  field. Positions of the fitted GMCs are labeled on the plot.

arms, similar to the  $^{13}\text{CO}(1-0)$ , while  $^{12}\text{CO}(1-0)$  comes from broad arms with abundant diffuse emission upstream from the arms. The less abundant isotopomers do not show the broad diffuse arms nearly as dramatically as the  $^{12}\text{CO}$  (Wright et al. 1993). Although the sensitivity of the  $\text{C}^{18}\text{O}(1-0)$  maps are not extremely high, the high sensitivity  $^{13}\text{CO}(1-0)$  line displays the same trend. These differences between  $^{12}\text{CO}$  and the rarer isotopes can be understood if the geometry and excitation of the nuclear gas clouds are considered.

### 3.1.1. The Geometry of the Starburst

Figure 4 shows that the two molecular arms in the nucleus of IC 342 progress inward and wrap around the central starburst. The arms appear to terminate in a partial ring surrounding the burst. If the two arms are caused by trailing density waves with orbital motions predicted for barred spiral arms outside of the Inner Lindblad Resonance (ILR) (e.g., Roberts, Huntley, & van Albada 1979; Athanassoula 1992), then the velocity pattern implies the northern arm is behind the starburst in projection and the southern arm is in front. Comparisons of  $\text{H}\alpha$  to thermal radio continuum and observations of  $\text{B}\gamma/\text{H}\alpha$  confirm that extinction toward the southern portion of the starburst complex is substantially higher than toward the north (Fig. 4; Fig. 5 of MTH00; Böker et al. 1997).

This geometry implies that, from our perspective, we are seeing the “starburst lit” face of the molecular clouds when viewing the northern arm (seeing the surface photo-dissociation regions) and the “backside” of the molecular clouds for the southern arm (seeing the ambient molecular gas). For optically thick transitions, such as those of  $^{12}\text{CO}$ ,

the lines should appear brighter along the northern arm relative to the southern arm since they are sensitive to temperature effects (Turner et al. 1993) whereas the optically thin transitions will trace column density. Therefore this

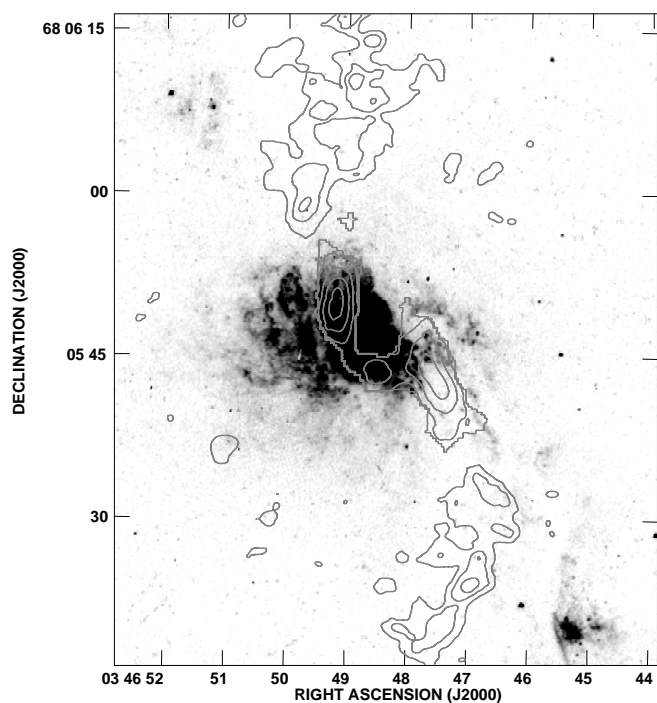


FIG. 4.—Total  $\text{H}_2$  column density maps as derived from  $\text{C}^{18}\text{O}$  (see text) overlaid on the *HST*  $\text{H}\alpha$  image of IC 342 (Gallagher et al 2001, in preparation). Contours are in steps of  $6.0 \times 10^{21} \text{ cm}^{-2}$ .

asymmetric pattern can manifest itself in optically thick transitions but not in transitions that are either inherently optically thin because of opacity or effectively thin because of large velocity gradients.

### 3.1.2. Giant Molecular Clouds in IC 342

Because of its low opacity and higher critical density,  $C^{18}O(2-1)$  emission, like  $^{13}CO(2-1)$ , is dominated by the dense giant molecular clouds (GMCs) seen in HCN emission (Downes et al. 1992). The  $C^{18}O(2-1)$  observations have the highest spatial resolution yet obtained ( $\sim 13$  pc) in IC 342, sufficient to resolve the nuclear GMCs into substructure. Therefore,  $C^{18}O(2-1)$  is used to derive the properties of the individual GMCs. Each cloud, identified only as a region of spatially and spectrally localized emission, not necessarily a gravitationally bound entity, has been fit with an elliptical Gaussian to determine its size, line width, location and intensity. Of the five GMCs identified by Downes et al., only GMCs A, B, C, and E are fit since GMC D is at the edge of the  $C^{18}O(2-1)$  primary beam. The four major GMCs are resolved into eight components (numbers are added to the letter designations in the case of substructure). The results of the fits are tabulated in Table 4.

All clouds are resolved (fitted sizes greater than half the FWHM of the beam size) except cloud C3. The GMCs are composed of several smaller clouds that are  $\sim 10 \times 30$  pc in size, with masses of about  $\sim 10^6 M_{\odot}$  and FWHM line widths of 20–30 K  $\text{km s}^{-1}$ . The GMCs tend to be non-spherical with axial ratios  $\sim 2$  and position angles generally oriented in the direction of the spiral arms. This is consistent with the presence of arm streaming motions over the nuclear region (Downes et al. 1992; TH92). Beam-averaged densities for the molecular clouds that make up the GMCs are  $\sim 10^{3.5} \text{ cm}^{-2}$  (§ 3.2.3). These values are quite similar to those found for the “envelope” of the Galactic center GMC, Sgr B2 (e.g., Gordon et al. 1993; Hüttemeister et al. 1995).

## 3.2. Comparing CO Isotopomers: Gas Excitation and Opacity in IC 342

### 3.2.1. Excitation Temperatures from $C^{18}O(2-1)/C^{18}O(1-0)$

Comparisons between rotational lines with different  $J$  states of optically thin transitions allow for the mapping of gas excitation temperatures ( $T_{\text{ex}}$ ). Generally, the main isotopomers of CO are optically thick in galactic nuclei and, as

such, are of little use in constraining  $T_{\text{ex}}$  (e.g., Braine & Combes 1992). Moreover, gradients in temperature over small scales appear to dominate the  $^{12}CO$  line ratios rather than  $T_{\text{ex}}$  (Turner et al. 1993). Optically thin line ratios, on the other hand, can be quite constraining, making the  $C^{18}O(2-1)/C^{18}O(1-0)$  line ratio a sensitive measure of  $T_{\text{ex}}$  in IC 342. The ratio of the  $C^{18}O(2-1)$  integrated intensity to the  $C^{18}O(1-0)$  intensity, under the LTE assumption is

$$\frac{\int^{18} T_{21} dv}{\int^{18} T_{10} dv} \approx \frac{{}^{18}f_{21} [{}^{18}J_{21}(T_{\text{ex}}) - {}^{18}J_{21}(T_{\text{cmb}})] (1 - e^{-18\tau_{21}})}{{}^{18}f_{10} [{}^{18}J_{10}(T_{\text{ex}}) - {}^{18}J_{10}(T_{\text{cmb}})] (1 - e^{-18\tau_{10}})}, \quad (1)$$

where  $J_{\nu}(T_{\text{ex}}) = (h\nu/k)/(\exp\{h\nu/kT_{\text{ex}}\} - 1)$ ,  $\tau$  and  $f$  are the optical depth and filling factor of each transition, respectively.

In Figure 5 (*left-hand panel*), the  $C^{18}O(2-1)/C^{18}O(1-0)$  line ratio map is presented for the nucleus of IC 342. Ratios of integrated intensities are used instead of the peak main-beam temperatures to increase the S/N. This requires that the  $C^{18}O(2-1)$  and  $C^{18}O(1-0)$  line profiles be the same. This is a good approximation (compare Figs. 1 and 2). In generating the ratio maps, the integrated intensity maps for  $C^{18}O(2-1)$  and  $C^{18}O(1-0)$  were convolved to matching beam sizes, divided, and blanked anywhere where emission was less than  $3\sigma$  in either map. Errors in the ratio maps are conservatively estimated to be  $\leq 35\%$  in magnitude and  $\leq 1''$  in position.

Aside from the two peaks seen in the ratio map, the  $C^{18}O(2-1)/C^{18}O(1-0)$  ratio map has relatively constant values of 0.7–1.3 over much of the central mapped region, with lower values preferentially found in the south. The highest  $C^{18}O(2-1)/C^{18}O(1-0)$  peak, with a value of 2.2, is found at the starburst region. The heating source for the warm molecular gas at this location is probably the massive stars of the starburst. The second ratio peak is at GMC A. GMC A is unusual in that it is not near either of the major radio continuum sources (§ 3.3), which suggests that the heating of GMC A is not caused by star formation. Some dynamical heating mechanism may be at work here, such as shock heating caused by large-scale bar-driven gas flows, which is consistent with the fact that it is the GMC closest to the dynamical center of the galaxy and to the ring of hot shocked gas seen in  $H_2$  (Böker et al. 1997).

A map of  $T_{\text{ex}}$  for the nuclear region derived using the  $C^{18}O(2-1)/C^{18}O(1-0)$  ratio is displayed in Figure 5 (*middle*

TABLE 4  
GIANT MOLECULAR CLOUDS IN IC 342

| Cloud    | $\alpha_{\text{ra}}, \delta_{\text{dec}}$<br>(03 <sup>h</sup> 46 <sup>m</sup> ; 68 <sup>s</sup> .05) | $a \times b$ ; p.a.<br>(pc $\times$ pc; deg) | $\Delta v_{1/2}$<br>(km $\text{s}^{-1}$ ) | $M_{\text{vir}}$<br>( $10^6 M_{\odot}$ ) | ${}^{\text{vir}}\langle N_{H_2} \rangle^b$<br>( $10^3 \text{ cm}^{-3}$ ) | $M_{C^{18}O}^c$<br>( $10^6 M_{\odot}$ ) |
|----------|--|--|---|--|--|---|
| A .....  | 48.51; 43.4  | 29 $\times$ 10; 78 $^{\circ}$                | 25  | 1.4                                      | 5.8  | 0.48                                    |
| B1 ..... | 47.80; 46.5  | 18 $\times$ 14; 0 $^{\circ}$ 7               | 15  | 0.46                                     | 2.3  | 0.94                                    |
| B2 ..... | 47.77; 45.5  | 29 $\times$ 7.8; 30 $^{\circ}$               | 21  | 0.86                                     | 5.2  | ...                                     |
| C1 ..... | 49.15; 51.3  | 22 $\times$ 16; 17 $^{\circ}$                | 27  | 1.8                                      | 5.6  | 1.2                                     |
| C2 ..... | 49.19; 49.5  | 39 $\times$ 8.7; 180 $^{\circ}$              | 26  | 1.6                                      | 5.2  | ...                                     |
| C3 ..... | 49.16; 46.9  | 37 $\times$ 0; 20 $^{\circ}$ <sup>a</sup>    | 29  | <1.7                                     | <9.3   | ...                                     |
| E1 ..... | 47.53; 42.7  | 28 $\times$ 12; 34 $^{\circ}$                | 19  | 0.90                                     | 3.0  | 1.0                                     |
| E2 ..... | 47.45; 41.2  | 19 $\times$ 16; 140 $^{\circ}$               | 15  | 0.54                                     | 2.1  | ...                                     |

NOTE.—Units of right ascension are in seconds, and units of declination are in arcseconds.

<sup>a</sup> The cloud is considered unresolved since the Gaussian fit size is less than half of the beam minor axis of 1 $^{\prime}$ .5 (13 pc).

<sup>b</sup> Average density assumes that the cloud is an ellipsoid of line-of-sight dimension,  $\ell \approx 1.4(ab)^{1/2}$ .

<sup>c</sup> Values represent the masses for the whole GMCs since substructure is not resolved in  $C^{18}O(1-0)$ .

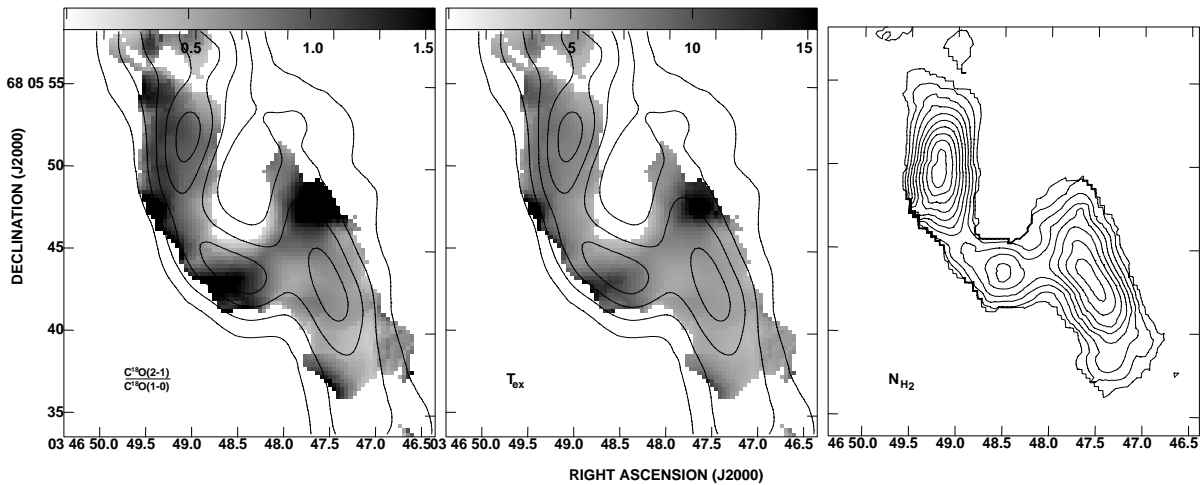


FIG. 5.—Gas excitation maps. Locations with integrated intensities below  $3\sigma$  in either of the generating maps are blanked. (Left)  $C^{18}O(2-1)/C^{18}O(1-0)$  line ratio map. Gray-scale range is 0–1.5, with a peak value of 2.2 at the location of the starburst. (Middle)  $T_{\text{ex}}$  derived from the  $C^{18}O(2-1)/C^{18}O(1-0)$  ratio (§ 3.2.1). Gray-scale range is 1–15 K, with a peak of 19 K. As a reference, the  $^{12}CO(1-0)$  integrated intensity map (contoured in steps of  $125 \text{ K km s}^{-1}$ ) is overlaid on each ratio map. (Right) Molecular gas column density derived from the  $C^{18}O(1-0)$  intensity map (Fig. 3, middle panel), the  $T_{\text{ex}}$  map in the middle panel here, and a  $[H_2/C^{18}O]$  abundance ratio of  $2.94 \times 10^6$ . Contours are in steps of  $2.5 \times 10^{20} \text{ cm}^{-2}$ , starting with  $7.5 \times 10^{20} \text{ cm}^{-2}$ .

panel).  $T_{\text{ex}}$  ranges from 7 to 10 K over much of the mapped region. The  $T_{\text{ex}}$  of the gas near the starburst region is  $19 \pm 8$  K. The secondary  $T_{\text{ex}}$  peak at GMC A has  $T_{\text{ex}} = 13 \pm 4$  K. Excitation temperatures derived from the  $C^{18}O$  transitions are lower than those estimated from  $^{13}CO$  (MTH00). We estimate filling factors using  $^{18}f_{10} \simeq T_{\text{mb}}/T_{\text{ex}}\tau_{10}$ . For  $T_{\text{ex}} \simeq 10$  K and  $\tau_{10} \sim 0.1$ – $0.2$  (§ 3.2.4), the implied filling factors are  $^{18}f_{10} \sim 0.5$ – $1$ , which, given the different beam sizes, are consistent with those found for  $^{13}CO$ . This implies that the  $C^{18}O(2-1)$  emission detected arises predominately from the same molecular gas component as the  $^{13}CO(2-1)$  emission (MTH00).

### 3.2.2. Molecular Gas Opacities and Abundances: $^{12}CO(1-0)/C^{18}O(1-0)$ and $^{13}CO(1-0)/C^{18}O(1-0)$

Comparison of the abundant and optically thick  $^{12}CO$  line with its less abundant and thinner cousins,  $^{13}CO$  and  $C^{18}O$ , can be used to trace optical depths and place limits on isotopic abundances. The isotopic line ratios are displayed in Figure 6 and Table 3. All of the isotopic line ratios discussed in this paper are between the (1–0) transitions of each isotopomer, so we suppress the (1–0) notation for the remainder of the paper. The  $^{12}CO/C^{18}O$  line ratio ranges from 11 to  $\gtrsim 110$  over the mapped region. Regions that are blanked because of low S/N tend to correspond to high  $^{12}CO/C^{18}O$  ratios since the weakness of the  $C^{18}O(1-0)$  line is the limiting factor. At the sites of the GMCs,  $^{12}CO/C^{18}O$  ratios of 30–60 are found, while values for  $^{13}CO/C^{18}O$  are 5–6. Typical Galactic center values for the  $^{12}CO/C^{18}O$  and  $^{13}CO/C^{18}O$  are  $\sim 60$ – $80$  and  $\sim 10$ , respectively (e.g., Oka et al. 1998; Dahmen et al. 1998). As in the Galactic center (Dahmen et al. 1998), variations in this ratio in the nucleus of IC 342 are substantial over small ( $\sim 30$  pc) spatial scales. The highest column-density regions at peaks B, C, and E tend to have the lowest isotopic ratios. This is expected since these are presumably the optically thickest regions.

The central trough region has surprisingly low values of  $^{12}CO/C^{18}O$  and  $^{13}CO/C^{18}O$  line ratios. The central trough region, which is a site of weak emission in all observed

transitions, is the only firmly established region of optically thin  $^{13}CO$  gas over the central distribution (MTH00). As such, it is expected to have high isotopic ratios and give the actual  $^{13}CO/C^{18}O$  isotopic abundance ratios. Surprisingly, both isotopic ratios,  $^{12}CO/C^{18}O = 24$  and  $^{13}CO/C^{18}O = 3.2$ , are lower here than the average across the rest of the spiral arms ( $C^{18}O$  overluminous). Along the spiral arms, the  $^{12}CO$  tends to dominate  $C^{18}O$  (highest ratios) on the upstream sides of the arms.  $C^{18}O$  becomes relatively more prominent as one moves toward the leading edge of the spiral arms (low ratios). The same effect is seen in  $^{12}CO/^{13}CO$  observations with higher sensitivity to extended structure (Wright et al. 1993).

Much of the structure seen in the isotopic ratio maps appear to be caused by excitation effects. The peak in the  $^{12}CO/C^{18}O$  ratio map at GMC A and toward the starburst near GMC B result from depopulation of the 1–0 level in the optically thin  $C^{18}O$  because of the increased  $T_{\text{ex}}$ , as confirmed by the high  $C^{18}O(2-1)/C^{18}O(1-0)$  ratios. The trend of decreasing ratio counterclockwise across the arms likely results from changes in density across the spiral arm caused by the density wave (Wright et al. 1993). The variation in excitation demonstrates the importance of observing higher  $J$  transitions when dealing with optically thin transitions. If one relies, as is often the case for extragalactic studies, on just the observations of the (1–0) transition of CO and its isotopomers, it is possible that variations in excitation can be mistaken for variations in morphological structure or column density.

A lower limit to the true  $^{12}CO/C^{18}O$  abundance ratio can be estimated from the observed ratio. In the limit of both transitions being optically thin (LTE), the isotopic line ratio will reflect the true isotopic abundance ratio. Since  $^{12}CO(1-0)$  is not optically thin, the ratio is a lower limit. For conservative lower limits to  $[^{12}C/^{13}C]$  and  $[^{16}O/^{18}O]$ , we take the highest (trustworthy) values of the ratio. The highest observed value of the  $^{12}CO/C^{18}O$  line ratio is  $\simeq 110$ . The  $[^{16}O/^{18}O]$  abundance ratio must be higher than this. The peak values of the  $^{13}CO/C^{18}O$  line ratio are

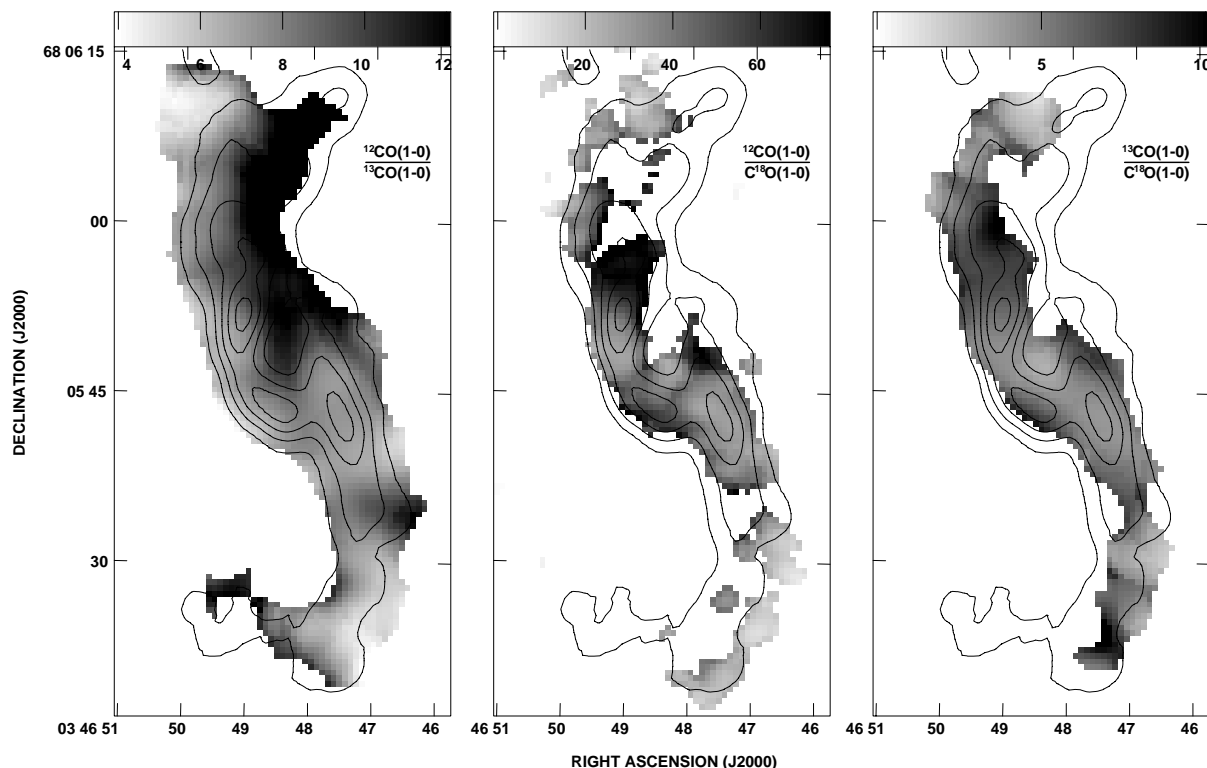


FIG. 6.—CO isotopic line ratio maps. Locations with integrated intensities below  $3\sigma$  in either of the generating maps are blanked. (Left)  $^{12}\text{CO}(1-0)/^{13}\text{CO}(1-0)$  ratio map (Wright et al 1993; MTH00). Gray scale ranges from 4 to 12 with darker shades corresponding to higher ratios. (Middle)  $^{12}\text{CO}(1-0)/\text{C}^{18}\text{O}(1-0)$  line ratio map, with the gray scale ranging from 0 to 75. (Right)  $^{13}\text{CO}(1-0)/\text{C}^{18}\text{O}(1-0)$  line ratio map, with a gray-scale range of 0–10. The  $^{12}\text{CO}(1-0)$  contours of Fig. 5 are shown for reference. For maps that include the  $^{13}\text{CO}(1-0)$  transition, the beam size is  $4.78 \times 3.79$  (MTH00), while the others are those of  $\text{C}^{18}\text{O}(1-0)$ .

about 11. However, both of these values are overestimates because of the non-LTE effects discussed in § 3.2.4. When we have corrected for the non-LTE effects, we estimate  $[\text{C}^{18}\text{O}/\text{C}^{16}\text{O}] > 110$  and  $[\text{C}^{13}\text{C}/\text{C}^{12}\text{C}] > 20$ . Though not well constrained, the values are consistent with those assumed as well as the (also weakly constrained) values previously estimated for IC 342 based on other molecular species (Henkel et al. 1998).

The low isotopic ratios seen toward the central trough appear to require truly anomalous abundances. The low ratios in this region imply that  $\text{C}^{18}\text{O}$  is overabundant relative to  $^{12}\text{CO}$  and  $^{13}\text{CO}$ . Neither isotope-selective photodissociation nor isotope-selective fractionation can be the explanation because in both cases the abundance of  $^{12}\text{CO}$  and  $^{13}\text{CO}$  are predicted to be larger relative to  $\text{C}^{18}\text{O}$ , not smaller (Langer et al. 1980; Langer et al. 1984; van Dishoeck & Black 1988). This makes the most likely possibility for the higher abundance of  $\text{C}^{18}\text{O}$  enrichment from  $^{18}\text{O}$  rich, massive star ejecta. A complete knowledge of the cooking sites of  $^{18}\text{O}$  has yet to be achieved, but it appears that  $^{18}\text{O}$  is a secondary product of massive stars (see, e.g., Wilson & Matteucci 1992; Henkel & Mauersberger 1993; Wilson & Rood 1994; Prantzos, Aubert, & Audouze 1996). If the central starburst is biased toward massive stars, a relative increase in the abundance of  $^{18}\text{O}$  (and hence  $\text{C}^{18}\text{O}$ ) is possible. Low  $^{12}\text{CO}/\text{C}^{18}\text{O}$  values have been found before in other starburst galaxies, such as NGC 253, M82, NGC 4945, as well as the AGN NGC 1068 (e.g., Henkel & Mauersberger 1993; Mauersberger et al. 1996; Papadopoulos et al. 1996). Using a chemical evolution model,

Henkel & Mauersberger (1993) have modeled the isotopic abundance ratio for a starburst typical of a galactic nuclei like those of M82, NGC 253, and possibly IC 342. They find that the  $[\text{C}^{18}\text{O}/\text{C}^{16}\text{O}]$  can drop as low as  $\sim 150$ . IC 342 also has a rather high  $\text{C}^{18}\text{O}(1-0)/\text{C}^{17}\text{O}(1-0)$  line ratio of 6.5, which is consistent with enhanced  $^{18}\text{O}$  (L. Sage, from Henkel et al. 1994). Therefore, for the central trough region, it is possible that the  $[\text{C}^{18}\text{O}/\text{H}_2]$  abundance may be higher than has been assumed.

### 3.2.3. Molecular Gas Density: $\text{C}^{18}\text{O}$ LVG Modeling

A sample of large velocity gradient (LVG) radiative transfer models were run to relate the observed intensities and line ratios to the physical properties of the cloud,  $n_{\text{H}_2}$  and  $T_k$  (e.g., Goldreich & Kwan 1974; Scoville & Solomon 1974; de Jong et al. 1975). LVG models probably are not appropriate for all lines in these tidally disturbed clouds (Turner et al. 1993; MTH00) but are nonetheless instructive, particularly when the transitions get optically thinner, as is the case for  $^{13}\text{CO}$  and  $\text{C}^{18}\text{O}$ . The LVG model used is the same as discussed in MTH00, except a  $[\text{C}^{18}\text{O}/\text{H}_2]$  abundance of  $3.4 \times 10^{-7}$  is used (§ 4.1). The ratio of cloud line width to cloud size is used to constrain the velocity gradient for the models (Table 4). Typical values of the velocity gradients for the GMCs are  $\sim 1\text{--}5 \text{ km s}^{-1} \text{ pc}^{-1}$ . In Figure 7, we display two models with velocity gradients of  $\sim 1$  and  $5 \text{ km s}^{-1} \text{ pc}^{-1}$ , for both  $^{13}\text{CO}$  and  $\text{C}^{18}\text{O}$  (see MTH00 for details of the  $^{13}\text{CO}$  models).

Since  $\text{C}^{18}\text{O}$  is optically thinner than  $^{13}\text{CO}$ , it is affected less by radiative trapping and thermalizes at a slightly

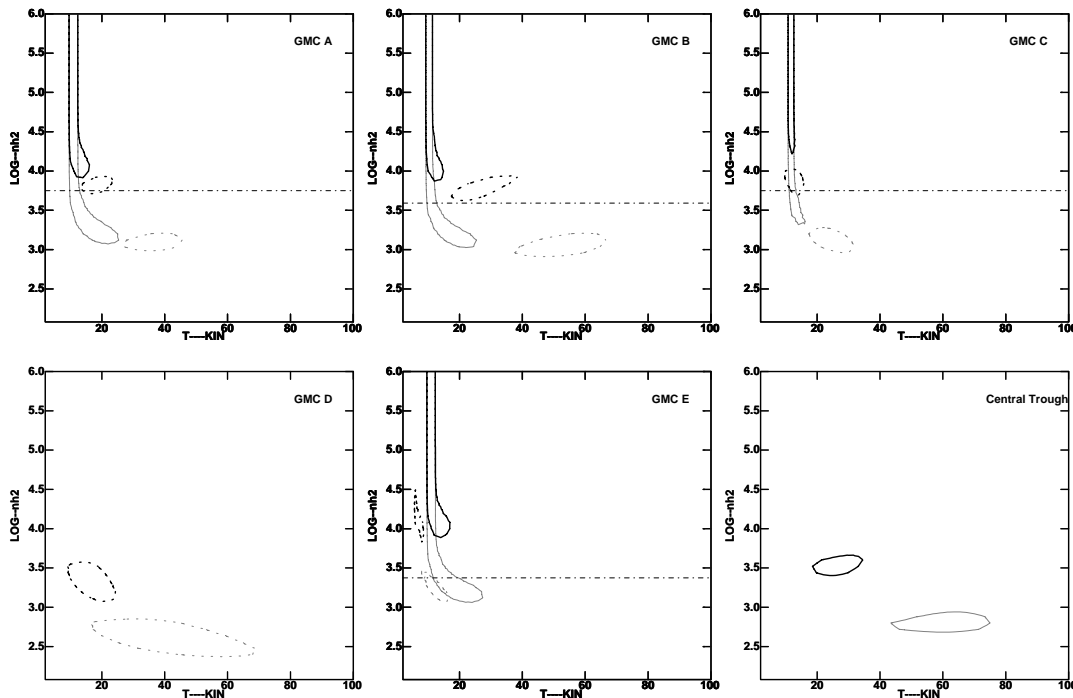


FIG. 7.—LVG model solutions for six nuclear locations. Contoured region represents the  $1\sigma$  confidence solution for the observed antenna temperature and  $(2-1)/(1-0)$  ratio. Solutions are displayed for both  $^{13}\text{CO}$  (black line; MTH00) and  $\text{C}^{18}\text{O}$  (gray line), with two assumed values of  $X_{\text{CO}}/dv/dr$ . Abundance ratios of  $[^{13}\text{CO}/\text{H}_2] = 2.1 \times 10^{-6}$  and  $[\text{C}^{18}\text{O}/\text{H}_2] = 3.4 \times 10^{-7}$  are assumed. Solid lines are the solutions for  $dv/dr = 1 \text{ km s}^{-1} \text{ pc}^{-1}$  ( $X_{^{13}\text{CO}}/dv/dr = 10^{-5.68}$ ;  $X_{\text{C}^{18}\text{O}}/dv/dr = 10^{-6.47}$ ), consistent with the data (Table 4). Dashed lines are solutions for  $dv/dr = 5 \text{ km s}^{-1} \text{ pc}^{-1}$  ( $X_{^{13}\text{CO}}/dv/dr = 10^{-6.38}$ ;  $X_{\text{C}^{18}\text{O}}/dv/dr = 10^{-7.17}$ ). Solutions are based on  $4''.8 \times 3''.9$  resolution and a filling factor of 0.25 for both  $^{13}\text{CO}$  and  $\text{C}^{18}\text{O}$  (MTH00; Table 4). A decrease of a factor of 2 in filling factors will shift the solution up ( $\sim 0.4$  dex) and to the left ( $\sim 10 \text{ K}$ ). Dot-dashed lines show the beam-averaged density estimated via the virial theorem for each GMC (using the full  $\text{C}^{18}\text{O}(2-1)$  resolution data; Table 4).

higher density than the corresponding lines of  $^{13}\text{CO}$ . LVG modeling of  $\text{C}^{18}\text{O}$  may be capable of constraining the densities, whereas  $^{13}\text{CO}$  has provided only lower limits to the density. Best-fit solutions obtained from the  $\text{C}^{18}\text{O}$  temperatures and line ratios are indeed close to the lower end of the solution range found in  $^{13}\text{CO}$  and are well constrained. The  $\text{C}^{18}\text{O}$  observations imply that most of the central GMCs have  $\langle n_{\text{H}_2} \rangle \simeq 10^{3.0-3.5} \text{ cm}^{-3}$  and  $T_k \simeq 10-40 \text{ K}$ . These moderate densities come directly from the fact that  $T_{\text{ex}}$  derived from  $\text{C}^{18}\text{O}$  are lower than those derived from  $^{13}\text{CO}$ . These densities are slightly smaller than those implied from the HCN observations (Downes et al. 1992), probably indicating that there is some further clumping that is not resolved. Closer inspection shows that, on average, the  $\text{C}^{18}\text{O}$  solutions for GMCs A, B, and C imply slightly warmer, lower density gas than does  $^{13}\text{CO}$ . This probably is caused by the fact that  $^{13}\text{CO}$  and  $\text{C}^{18}\text{O}$  were assumed to have the same filling factor (0.25 over a  $4''.8 \times 3''.9$  beam; MTH00). Since the critical density is higher for  $\text{C}^{18}\text{O}$ , one might expect cloud sizes to be slightly smaller for  $\text{C}^{18}\text{O}$  than for  $^{13}\text{CO}$ . If the relative filling factor for the  $\text{C}^{18}\text{O}$  emitting gas is lowered, the models become consistent for all locations. In every case, the decrease in filling factor required for agreement between  $^{13}\text{CO}$  and  $\text{C}^{18}\text{O}$  is less than a factor of 2. It is interesting to compare the average densities derived from the LVG analysis with what is predicted from high-resolution  $\text{C}^{18}\text{O}(2-1)$  and the virial theorem (§ 4.1). The densities estimated from both methods are not too different, with the values derived from the virial theorem tending to be about 1.5–3 times larger than the LVG models.

### 3.2.4. Isotopic Line Ratios: Complications and Important Considerations

These multiline, multitransition data on IC 342 provide a wealth of information on the complex interactions between opacity and temperature for molecular clouds in starburst environments. Here we consider what these multitransition studies as a whole indicate for the opacities of the CO lines. The magnitude and effect of several different non-LTE effects are estimated for the nucleus of IC 342.

For IC 342, the  $T_{\text{ex}}$  and filling factors derived from the  $^{12}\text{CO}$ ,  $^{13}\text{CO}$ , and  $\text{C}^{18}\text{O}$  lines can depend on the transition considered. A single  $T_{\text{ex}}$  or filling factor cannot be assumed for all the lines. This complicates the determination of opacities and abundances from the line ratios. Since  $^{13}\text{CO}$  and  $\text{C}^{18}\text{O}$  have lower opacities, their effective critical densities are higher than for  $^{12}\text{CO}$ . They are more confined to the cloud cores and will have smaller relative filling factors (Wall & Jaffe 1990; MTH00). For the externally heated clouds in IC 342, the  $^{12}\text{CO}$  transitions will also have higher  $T_{\text{ex}}$  than the optically thin species (Turner et al. 1993; MTH00). Therefore the isotopic ratios between  $^{12}\text{CO}$  and other isotopomers assuming LTE will underestimate the line opacities.

It is difficult to estimate the degree to which differing filling factors impact the line ratios independent of the opacity. However, differences in the  $T_{\text{ex}}$  can be estimated since values of  $T_{\text{ex}}$  have been derived separately for  $^{12}\text{CO}$ ,  $^{13}\text{CO}$ , and  $\text{C}^{18}\text{O}$  (Turner et al. 1993; MTH00; § 3.2.1). If the peak brightness temperature of the  $^{12}\text{CO}(2-1)$  transition is taken as a lower limit to the  $^{12}T_{\text{ex}}$ , the  $^{13}\text{CO}(2-1)/^{13}\text{CO}(1-0)$  line ratio under the optically thin assumption to

estimate the  $^{13}T_{\text{ex}}$ , and similarly the  $\text{C}^{18}\text{O}(2-1)/\text{C}^{18}\text{O}(1-0)$  line ratio for the  $^{18}T_{\text{ex}}$ , then the magnitude of the temperature differences can be estimated. Over the central GMCs, typical derived temperatures are  $^{12}T_{\text{ex}} \gtrsim 26$  K,  $^{13}T_{\text{ex}} \simeq 20$  K, and  $^{18}T_{\text{ex}} \simeq 10$  K. This implies that the line ratios involving  $\text{C}^{18}\text{O}$  are  $\sim 2-3$  times larger than expected assuming the same excitation temperature applies for all transitions. Taking into account these corrections, the isotopic line ratios imply  $^{13}\tau_{10} \sim 0.7-3$  ( $^{18}\tau_{10} \sim 0.1-0.5$ ). These results are consistent with  $^{13}\tau_{10} \gtrsim 1$  as was previously found from the  $^{13}\text{CO}$  line ratios (MTH00). When one compares isotopic line ratios in IC 342 to find abundances and opacities, the derived values are underestimates because the optically thinner transitions have lower  $T_{\text{ex}}$  than the thicker transitions. We expect that this variation in  $T_{\text{ex}}$  for CO lines of different opacities may be common in other starburst nuclei and should be taken into account when making estimates of opacities and abundances.

### 3.3. Millimeter Continuum Morphology

Continuum emission was detected at 2.6 and 1.3 mm in IC 342 in a 1 GHz continuum channel. The 2.6 and 1.3 mm continuum maps, convolved to the same beam size, are displayed in Figure 8, (*top left and right panels*). The 2.6 mm continuum emission shows a twin-peaked structure similar in morphology to the 2 cm and 3.4 mm continuum emission (Turner & Ho 1983; Downes et al. 1992). The two strongest sites of millimeter continuum are coincident with the nuclear starburst (near GMC B) and a secondary cluster centered on GMC C, respectively. The peak intensity of 2.6 mm continuum is  $4.4 \text{ mJy beam}^{-1}$ .

Figure 8 (*bottom left and right panels*) displays the spectral index between 2 cm/2.6 mm and 2.6 mm/1 mm over the central region. The 2 cm to 2.6 mm spectral index ranges from  $\alpha_{2.6}^2 \simeq -0.4$  to 0.3 ( $S_\nu \propto \nu^\alpha$ ) over the map, similar to what is found for the spectral index between 6 and 2 cm

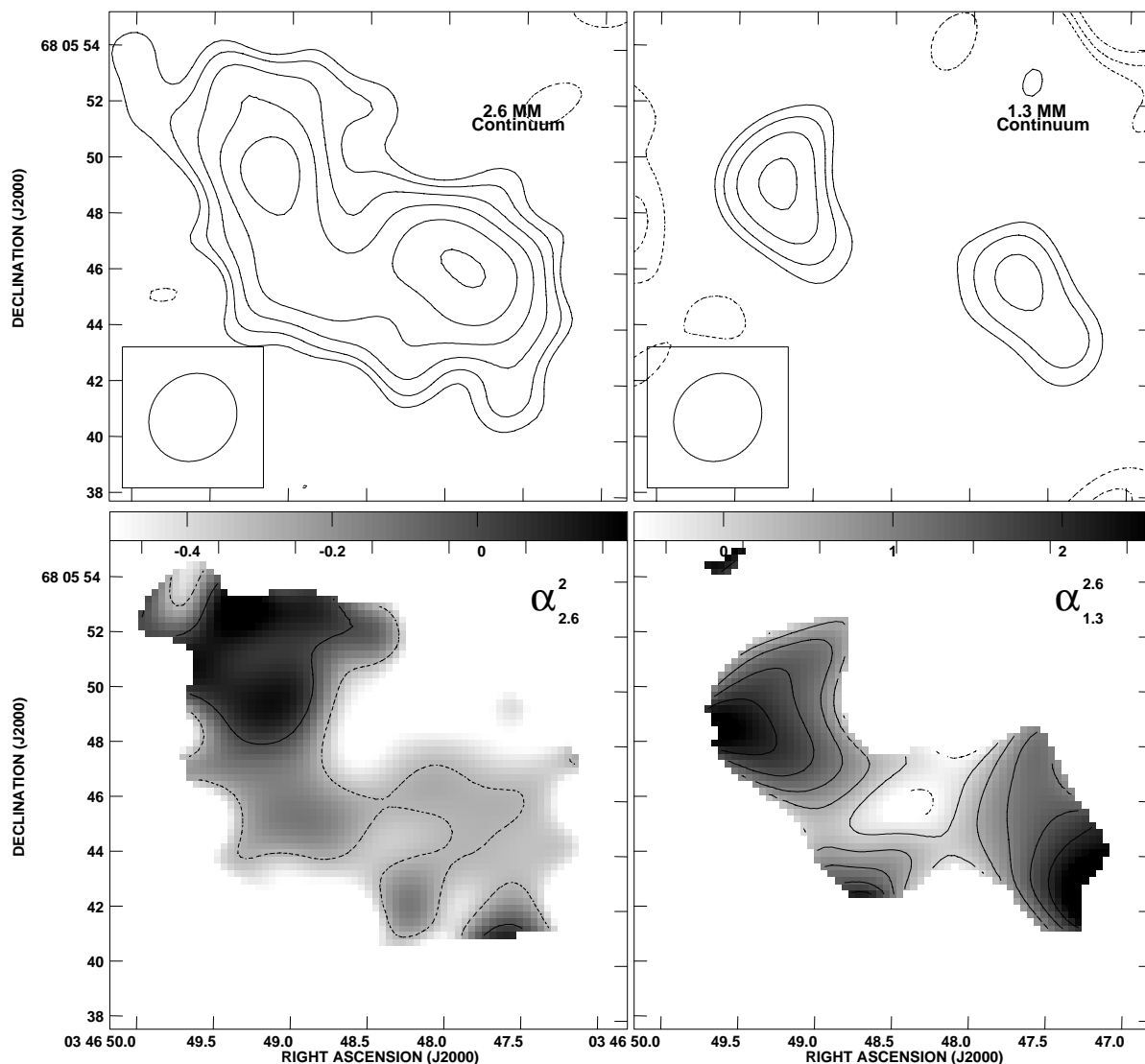


FIG. 8.—3 and 1.3 mm continuum maps. (*Top left*) 2.6 mm (110 GHz) continuum emission. Contours are  $2^{0.5i}$  ( $i = 0, 1, 2, \dots$ ) times the  $2\sigma$  value of  $0.4 \text{ mJy beam}^{-1}$ . (*Top right*) 1.3 mm (220 GHz) continuum emission. Contour levels are the same as 2.6 mm, with a  $2\sigma$  value of  $4.0 \text{ mJy beam}^{-1}$ . Both maps are displayed at the same resolution (3 mm). (*Bottom left*) 2 cm/2.6 mm spectral index map ( $S \propto \nu^\alpha$ ). (*Bottom right*) 2.6 mm/1 mm spectral index map. For the two spectral index maps, darker gray scales represent larger values. Contours are in steps of 0.25 for the bottom left panel and 0.5 for bottom right panel. Negative contours are dashed. The maps are blanked when 2.6 mm continuum is less than  $0.4 \text{ mJy beam}^{-1}$  (*bottom left*) and when 1.3 mm continuum is less  $2.0 \text{ mJy beam}^{-1}$  (*bottom right*).

(Turner & Ho 1983). The generally flat spectrum over the nuclear region is consistent with thermal bremsstrahlung emission. Lower values of  $\alpha_{2.6}^2$  ( $\sim -0.4$ ) toward the northwest side of the central ring imply some contamination by nonthermal synchrotron emission at 2 cm in this region. Toward GMC C,  $\alpha_{2.6}^2$  is  $\sim +0.2$  to  $+0.3$ . Assuming all the 2.6 mm continuum emission is from bremsstrahlung, the implied number of ionizing photons,  $N_{\text{uv}}$ , present at each peak is  $\simeq 1.8 \times 10^{51} \text{ s}^{-1}$  or about 80 O6 stars (assuming a  $T_e = 8000 \text{ K}$ ; e.g., Mezger & Henderson 1967; Vacca, Garmany, & Shull 1996). The total flux in the mapped region is  $S_{2.6\text{mm}} = 26 \text{ mJy}$ , implying that the entire central star-forming region ( $\sim 75 \text{ pc}$ ) has  $N_{\text{uv}} \simeq 10^{52} \text{ s}^{-1}$  ( $\sim 460 \text{ O6}$  stars; consistent with that estimated by Becklin et al. 1980; Turner & Ho 1983; Downes et al. 1992).

The 1.3 mm continuum emission is detected only from the molecular column density peaks as traced by  $\text{C}^{18}\text{O}$  because the S/N is lower at this frequency. Peak 1.3 mm intensities are  $8 \text{ mJy beam}^{-1}$  ( $\sim 4 \sigma$ ) and  $12 \text{ mJy beam}^{-1}$  ( $\sim 6 \sigma$ ) for GMC B and C, respectively. Both 1.3 mm continuum sources have rising spectral indices of  $\alpha_{2.6}^{1.3} \sim +2.5$  between 2.6 and 1.3 mm. Rising spectral indices at 1.3 mm are seen tentatively toward GMC A as well (Fig. 8, *bottom right*). The 1.3 mm continuum appears to be largely made up of thermal dust emission. In fact, for GMC C, the slightly rising spectral index between 2 cm and 2.6 mm indicates that a small amount of dust emission may even contribute to the 2.6 mm continuum at this location ( $\lesssim 1 \text{ mJy beam}^{-1}$ ). We discuss the dust masses implied by the 1.3 mm continuum in the following section.

#### 4. DISCUSSION

To study the relation of galactic dynamics, molecular gas, and star formation, one needs accurate surface density maps of molecular gas. Estimates of column densities made using  $^{12}\text{CO}$  and a conversion factor,  $X_{\text{CO}}$  are commonplace but require  $X_{\text{CO}}$  to be valid, which is not yet established. Comparisons between masses estimated using various methods need to be made in order to investigate the validity of  $X_{\text{CO}}$  in starburst environments. Given the wealth of data available for IC 342, and in particular the valuable  $\text{C}^{18}\text{O}$  and 1.3 mm maps, accurate values of molecular column density can be obtained.

##### 4.1. $\text{H}_2$ Gas Column Densities: Comparing $\text{C}^{18}\text{O}$ , $X_{\text{CO}}$ , Virial Masses, and Dust

Since  $\text{C}^{18}\text{O}$  is optically thin,  $\text{H}_2$  column densities can be obtained from the total  $\text{C}^{18}\text{O}(1-0)$  intensity:

$$N(\text{H}_2)_{\text{C}^{18}\text{O}} = 2.42 \times 10^{14} \text{ cm}^{-2} \frac{[\text{H}_2]}{[\text{C}^{18}\text{O}]} \times \frac{e^{(5.27/T_{\text{ex}})}}{(e^{(5.27/T_{\text{ex}})} - 1)} I_{\text{C}^{18}\text{O}} (\text{K km s}^{-1}). \quad (2)$$

We adopt an abundance ratio of  $[\text{H}_2]/[\text{C}^{18}\text{O}] = 2.94 \times 10^6$  or  $[\text{C}^{16}\text{O}]/[\text{C}^{18}\text{O}] = 250$  (Frerking, Langer, & Wilson 1982; Henkel et al. 1994; Wilson & Rood 1994). Figures 4 and 5 (*right-hand panel*) show a map of  $N_{\text{H}_2}$  calculated from optically thin  $\text{C}^{18}\text{O}$ . Within the 2–1 primary beam, the derived  $T_{\text{ex}}$  obtained from the  $\text{C}^{18}\text{O}(2-1)/\text{C}^{18}\text{O}(1-0)$  line ratios are used in calculating the column density. Since  $T_{\text{ex}}$  was determined to be  $\sim 7-10 \text{ K}$  (§ 3.2.1),

$T_{\text{ex}} = 10 \text{ K}$  is assumed when deriving column densities for regions outside the  $\text{C}^{18}\text{O}(2-1)$  primary beam. Column densities measured in the central region of IC 342 range from less than  $0.25-4.8 \times 10^{22} \text{ cm}^{-2}$  (corrected for resolved out flux assuming a uniform distribution). These values obtained for optically thin  $\text{C}^{18}\text{O}$  can be compared with column densities estimated using a Galactic disk  $X_{\text{CO}}$  of  $\simeq 2 \times 10^{20} \text{ cm}^{-2} (\text{K km s}^{-1})^{-1}$  (Strong et al. 1988; Hunter et al. 1997). Using  $X_{\text{CO}}$ , we obtain  $N_{\text{H}_2}$  column densities in the range of  $2-12 \times 10^{22} \text{ cm}^{-2}$  over the  $\sim 25 \text{ pc}$  beam sizes, a factor of 3 to 13 higher than the column densities based on  $\text{C}^{18}\text{O}$ .

Two additional column density estimates are considered. First, since the GMCs in the center of IC 342 are resolved, the total molecular mass can be estimated from the virial theorem. For molecular clouds with density profiles given by  $\rho \propto R^{-\gamma}$ , the virial mass is given by (e.g., MacLaren, Richardson, & Wolfendale 1988)

$$M_v = 126 \left( \frac{5 - 2\gamma}{3 - \gamma} \right) \left( \frac{\Delta v_{1/2}}{\text{km s}^{-1}} \right)^2 \left( \frac{R}{\text{pc}} \right), \quad (3)$$

where  $R$  is the radius of the cloud and  $\Delta v_{1/2}$  is the FWHM of the line width. The radius of the clouds is assumed to be  $1.4R_{1/2}$ , or  $0.7 (ab)^{1/2}$  (e.g., Wilson & Scoville 1990; Goldsmith, Bergin, & Lis 1997), where  $a$  and  $b$  are the FWHM fitted sizes of the major and minor axes. A  $\gamma = 1$  is assumed for the GMCs, consistent with what is found for Galactic clouds (e.g., Cernicharo, Bachiller, & Duvert 1985; Scoville et al. 1987; MacLaren et al. 1988). However, the derived masses are only weakly dependent on the choice of  $\gamma$ . The masses will change from their  $\gamma = 1$  values by less than a factor of 50% for any  $\gamma$  between 0 and 2. Virial cloud masses for  $\gamma = 1$  are displayed in Table 4.

Gas masses may also be estimated from optically thin thermal dust continuum emission. The 2.6 and 1.3 mm continuum maps are used to measure the amount of dust. Assuming the clouds are entirely molecular and have a constant gas to dust ratio of 100 by mass, the gas mass is related to the 1.3 mm dust continuum flux by (e.g., Hildebrand 1983)

$$M_{\text{gas}}(1.3 \text{ mm}) = 310 M_{\odot} \left( \frac{S_{1.3\text{mm}}}{\text{mJy}} \right) \left( \frac{D}{\text{Mpc}} \right)^2 \times \left( \frac{\kappa_v}{\text{cm}^2 \text{ g}^{-1}} \right)^{-1} (e^{(10.56/T_d)} - 1), \quad (4)$$

where  $\kappa_v$  is the dust absorption coefficient at this frequency,  $S_{1.3\text{mm}}$  is the 1.3 mm flux,  $D$  is the distance, and  $T_d$  is the dust temperature. The dust opacity,  $\kappa_v$ , at 1.3 mm is taken to be  $3.1 \times 10^{-3} \text{ cm}^2 \text{ g}^{-1}$  but is uncertain by at least a factor of 4 (Pollack et al. 1994). A  $T_d = 42 \text{ K}$  is assumed based on the FIR colors (Becklin et al. 1980; Rickard & Harvey 1984). The dust temperature applicable to the 1.3 mm observations could be lower than this if a cool dust component missed by the FIR observations exists. Since dust emission is detected only at the two sites with major star formation, we do not expect that a substantial cool dust component exists here. Therefore, uncertainties in the derived gas mass are dominated by the uncertainty in opacity.

The amount of dust emission is estimated by assuming the 2.6 mm continuum emission is entirely thermal free-free emission. The nearly identical morphology and flat spectral

index between 2.6 mm and 2 cm makes this a reasonable assumption (Turner & Ho 1983). (In the youngest star-forming regions, there are regions of compact optically thick H II regions that do have rising spectral indices [e.g., Beck et al. 1996; Turner, Ho, & Beck 1998; Beck, Turner, & Kovo 2000], but even these regions will be optically thin by 3 mm.) Thermal free-free emission at 1.3 mm is removed by extrapolating the 2.6 mm map to 1.3 mm using  $\alpha = -0.1$ . The remaining flux of  $\sim 8$  mJy beam $^{-1}$  at GMC C and  $\sim 4$  mJy beam $^{-1}$  at GMC B is estimated to be dust emission. Beam-averaged column densities based on dust emission are shown in Table 5. The gas masses implied by the dust are  $7.4 \times 10^5$  and  $3.6 \times 10^5 M_\odot$  (or  $7.7 \times 10^{22}$  cm $^{-2}$  and  $3.8 \times 10^{22}$  cm $^{-2}$ ) for the two clouds detected at 1.3 mm, respectively. Uncertainties are at least a factor of 2–4, dominated by uncertainties in  $\kappa_v$ . Given the large uncertainties, dust masses should be treated as indicative only. Dust emission in IC 342 will be discussed further in a later paper (Meier et al. 2001, in preparation).

#### 4.2. The Validity of $X_{\text{CO}}$ in the Nuclear GMCs of IC 342

The different methods of obtaining  $M_{\text{H}_2}$  and  $N_{\text{H}_2}$  can now be compared to determine the validity of the  $X_{\text{CO}}$  in the nucleus of IC 342. Column densities derived for the GMCs in IC 342 from the three different methods described above are listed in Table 5. At all locations, the lowest column densities are estimated from the  $\text{C}^{18}\text{O}$  data. The  $\text{C}^{18}\text{O}$  column densities at the GMCs are 3–4 times lower than those found using the Galactic  $X_{\text{CO}}$ . Column densities based on dust emission are slightly higher but consistent with those estimated from  $\text{C}^{18}\text{O}$ . Column densities based on the virial theorem tend to be the largest of the three methods and are approximately equal to the values obtained using the Galactic  $X_{\text{CO}}$ .

The dominant uncertainties in the column density estimates based on the  $\text{C}^{18}\text{O}$  data are the  $[\text{C}^{18}\text{O}/\text{H}_2]$  abundance ratio and differing source sizes. A Galactic center value of  $[\text{C}^{18}\text{O}/\text{H}_2]$  has been assumed. The isotopic line ratios, while not strongly constrained, indicate that this value is reasonable (§ 3.2.2). For the  $\text{C}^{18}\text{O}$  column density to be consistent with  $X_{\text{CO}}$  value, an abundance of  $[\text{C}^{18}\text{O}/\text{C}^{16}\text{O}] \simeq 1000$  would be required. This value is larger than

the highest ISM values seen in the Galaxy ( $\sim 600$ ) and at least a factor of 4 larger than is typically seen in galactic nuclei (e.g., Henkel & Mauersberger 1993; Wilson & Rood 1994). If anything, the nucleus of IC 342 could have a  $[\text{C}^{18}\text{O}/\text{H}_2]$  abundance that is higher than the  $3.4 \times 10^{-7}$  assumed, since nuclear processing in massive stars tends to raise the  $[\text{C}^{18}\text{O}/\text{H}_2]$  abundance rather than lower it (§ 3.2.2). From an abundance standpoint, we expect that the  $\text{C}^{18}\text{O}$  values listed in Table 5 do not underestimate the molecular gas by a large amount. From a photochemical standpoint, it is possible, given isotope selective photodissociation and gas density variations, that  $\text{C}^{18}\text{O}$  emission will remain undetected in regions with detectable  $^{12}\text{CO}$ . In IC 342, the cloud sizes do appear to be smaller in  $\text{C}^{18}\text{O}$  than in  $^{12}\text{CO}$  (§ 3.2.3; MTH00), so the column densities estimated by  $\text{C}^{18}\text{O}$  cloud be slight underestimates. Gas excitation can also influence the optically thin estimates, although our dual line observations mostly correct for excitation.

Column densities estimated from the virial theorem are very likely overestimates of the true molecular gas column density. The clouds tend to be somewhat filamentary in appearance, consistent with tidal shear or arm streaming motions (TH92; Downes et al. 1992). The line widths of the GMCs are probably larger than virial and the clouds may not be bound. In addition, line widths in this region are slightly overestimated simply by the finite resolution of the telescope in the steep part of the rotation curve. Not surprisingly, therefore, the LVG models predict average densities a factor of 1.5–3 times lower than the virial prediction.

While the dust masses are more uncertain because of assumptions of  $T_d$  and opacity compared to the  $\text{C}^{18}\text{O}$  mass, they provide independent indications for a lower  $X_{\text{CO}}$  in the center of IC 342. First, the conversion factor estimated from dust continuum emission for GMCs B and C are intermediate between the Galactic  $X_{\text{CO}}$  value and the  $\text{C}^{18}\text{O}$  estimates. Second, using near-infrared (NIR) spectroscopy to measure the NIR extinction, Böker et al. (1997) obtain  $A_v \simeq 25$ . From the geometry of the starburst (§ 3.1.1), it appears that GMC B is in front of the starburst. The NIR extinction then implies a column density of  $\sim 2 \times 10^{22}$  cm $^{-2}$  toward the starburst region (using the Galactic con-

TABLE 5  
THE CONVERSION FACTOR IN IC 342

| Location             | $\text{C}^{18}\text{O}N_{\text{H}_2}$ <sup>a</sup><br>( $10^{22}$ cm $^{-2}$ ) | $\text{vir}N_{\text{H}_2}$ <sup>b</sup><br>( $10^{22}$ cm $^{-2}$ ) | $\text{dust}N_{\text{H}_2}$ <sup>c</sup><br>( $10^{22}$ cm $^{-2}$ ) | $X_{\text{CO}}N_{\text{H}_2}$ <sup>d</sup><br>( $10^{22}$ cm $^{-2}$ ) | $\left\langle \frac{X_{\text{MW}}}{X_{\text{C}^{18}\text{O}}} \right\rangle$ |
|----------------------|--|---|--|--|--|
| A .....              | 3.1  | 11  | $\sim 1.5$   | 15   | 4.8  |
| B .....              | 3.3  | 11  | 3.8  | 11   | 3.3  |
| C .....              | 4.8  | 13 <sup>f</sup>   | 7.7  | 16   | 3.3  |
| D .....              | 1.3  | ...   | ...  | 13   | 10   |
| E .....              | 3.7  | 12  | ...  | 15   | 4.1  |
| Arm .....            | 1.1 <sup>e</sup>   | ...   | ...  | 7.6  | 6.9  |
| Off-arm .....        | $< 0.55^e$   | ...   | ...  | 3.7  | $> 6.7$  |
| Central trough ..... | 1.1 <sup>e</sup>   | ...   | ...  | 5.1  | 4.6  |

<sup>a</sup> Using an assumed abundance of  $[\text{C}^{16}\text{O}/\text{C}^{18}\text{O}] = 250$  and correcting for the 67% missing flux.

<sup>b</sup> Based on the sum of the masses in each subcomponent within the  $^{12}\text{CO}$  beam size divided by 1.36  $\mu_{\text{H}_2}$  (to account for He) and averaged over the beam.

<sup>c</sup> Based on the dust mass,  $M_{\text{H}_2}(M_\odot)$  estimate averaged over the beam (§ 4.1).

<sup>d</sup> Using an  $X_{\text{CO}}(\text{MW}) = 2 \times 10^{20}$  cm $^{-2}$  K km s $^{-1}$ , and the  $^{12}\text{CO}(1-0)$  map in Fig. 3 (left-hand panel), corrected for the 25% missing flux.

<sup>e</sup> Assuming an excitation temperature of 10 K.

<sup>f</sup> Only component C2 is included; C1 and C3 are outside the  $^{12}\text{CO}(1-0)$  beam size.

version between column density and extinction). This value is roughly consistent with the optically thin  $C^{18}O$  value at this location. If some of the gas is behind the starburst, then this is an underestimate. But even if the starburst is in the middle of the cloud, the observed value is still below that estimated from  $X_{CO}$ .

Considering all the different methods, and their possible biases, it is concluded that  $X_{CO}(IC\ 342) \simeq 0.7\text{--}1 \times 10^{20} \text{ cm}^{-2} (\text{K km s}^{-1})^{-1}$  for the inner  $\sim 75$  pc of IC 342, or about one-half to one-third the value of  $X_{CO}$  for the Galaxy. While this value is not as low on average as is inferred for the Galactic center, it is closer to what is found toward the GMCs Sgr A and Sgr B2 in the Galactic center, based on  $C^{18}O$  (Dahmen et al. 1998).

#### 4.3. Variation of the $X_{CO}$ across the Nuclear Minispiral

Of equal importance to the mean  $X_{CO}$  in the center of IC 342 is its spatial variation and the general applicability of a constant  $X_{CO}$  over the nuclear region. As noted above, there are some differences between the morphology of the  $C^{18}O(1\text{--}0)$  and  $^{12}CO(1\text{--}0)$  emission.  $C^{18}O$  in the outer arm regions is fainter than predicted using even the modified  $X_{CO}$  suitable for the central GMCs, implying  $X_{CO}(IC\ 342)$  is even lower in the diffuse gas. Plotted in Figure 9 (Table 5) is the estimated variation in  $X_{CO}(IC\ 342)$  obtained from  $C^{18}O$  with distance from the dynamical center for regions with detected  $C^{18}O$ .  $X_{CO}(IC\ 342)$  decreases by  $\sim 2\text{--}3$  from the central value beyond the inner  $15''$ . For the diffuse gas behind the density wave,  $C^{18}O(1\text{--}0)$  emission is not detected at all and  $X_{CO}$  may be even lower.

Since the  $C^{18}O(2\text{--}1)$  observations do not cover this region, we have assumed  $T_{ex} = 10$  K, consistent with the average seen over the mapped region. Densities in the diffuse gas are probably lower than toward the GMCs, so it is possible that  $T_{ex}$  for  $C^{18}O$  could be slightly lower than this because of its higher critical density. Column densities estimated from the optically thin  $C^{18}O$  predict lower column densities for cooler temperatures (even larger difference in  $X_{CO}$ ). Moreover, derived  $N(H_2)$  are only weakly

sensitive to  $T_{ex}$  for such low temperatures (eq. [2]). Therefore, the possibility that  $C^{18}O$  is more strongly subthermal in these regions cannot be the explanation for the differences derived in the  $X_{CO}$ . This indicates that the widespread, diffuse gas seen over much of the mapped region is substantially brighter in  $^{12}CO$  than would be expected based on the  $C^{18}O$  data. Even higher values are found in the north, consistent with  $^{12}CO$  being especially bright in the north (§ 3.1.1).

Dahmen et al. (1998) find that diffuse gas in the Galactic center also has a much smaller  $X_{CO}$  than is estimated for Sgr A and Sgr B2, and that  $X_{CO}$  is not valid across the entire region. Because they did not have  $C^{18}O(2\text{--}1)$  observations to go along with  $C^{18}O(1\text{--}0)$  and instead relied on global LVG models to predict the  $C^{18}O$  excitation, some of the structure they find probably reflects variations in excitation. Such variations are important in IC 342 (§ 3.2.2). Hence, simply using a “modified”  $X_{CO}$  is only good enough to characterize the molecular gas distribution in nuclei to a factor of  $\sim 2$ , with the amount of diffuse gas being overestimated. Indications of similar variations in the estimated  $X_{CO}$  with distance from the center are also seen in M82 and Maffei 2 (Smith et al. 1991; Meier, Hurt, & Turner 2001, in preparation).

#### 4.4. An Unusually High Star Formation Efficiency: Dynamically Determined Star Formation in IC 342?

The revised  $H_2$  column densities have implications for the nature and efficiency of star formation in IC 342. Since  $^{12}CO$  appears to slightly overestimate the molecular column densities, previously derived molecular mass fractions for the central region of IC 342 need to be revised downward (e.g., TH92). Summing all the molecular gas (Fig. 5, right-hand panel) over the central  $\sim 90$  pc gives  $M_{H_2} \simeq 5.3 \times 10^6 M_{\odot}$  (corrected for He and “missing flux”). From the nuclear rotation curve, the estimated dynamical mass over the same region is  $M_{dyn} \simeq 5.7 \times 10^7 M_{\odot}$  (TH92), or  $M_{H_2}/M_{dyn} \simeq 10\%$ . The molecular mass fraction increases to  $M_{H_2}/M_{dyn} \simeq 30\%$  within the central 45 pc. If  $X_{CO}$  drops substantially outside of the central starburst region as indicated by the  $C^{18}O$  data, then the molecular arms do not make up a substantial percentage of the dynamical mass over the central arcminute.

The dynamics (and hence the molecular gas distribution) of the nuclear region are dominated by the stellar mass distribution. Recent NIR  $K$ -band images indicate that a small stellar bar (major axis  $\sim 110$  pc) is present in the nucleus (Böker et al. 1997). The molecular gas distribution probably reflects gas moving on barred orbits (Lo et al. 1984; Ishizuki et al. 1990; Böker et al. 1997). Using the  $^{13}CO$  observations, TH92 estimated that star formation efficiencies (SFE) toward the central starburst region and GMC B, in particular, are very high. They estimate based on  $N_{Ly\alpha}$  that, at the starburst, the total mass of newly formed stars with masses greater than  $1 M_{\odot}$ ,  $M_*$ , is  $\simeq 10^6 M_{\odot}$ . With our improved  $H_2$  mass for GMC B of  $M_{H_2} \simeq 4.0 \times 10^5 M_{\odot}$ , we obtain SFE of  $M_*/M_{H_2} \sim 2$ . This is an extremely high SFE. Alternatively, this could be an indication that the IMF is truncated above  $1 M_{\odot}$  or that the starburst is in the process of destroying its molecular cloud.

It is worth reemphasizing a point made by other studies that the sites of star formation in IC 342 are not strictly correlated with either the global molecular gas column density or molecular gas density (Ishizuki et al. 1990;

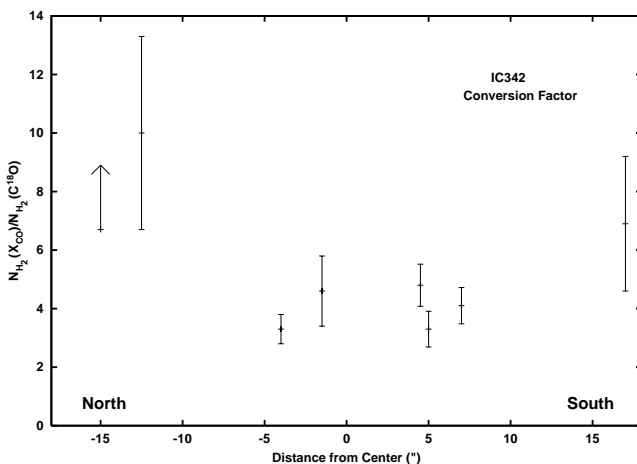


FIG. 9.—Ratio of the conversion factor found from  $C^{18}O$  observations in IC 342 vs. the Galactic value as a function of distance from the dynamical center of IC 342 (Table 1). Error bars reflect only the uncertainty in the  $C^{18}O$  integrated intensity and do not include systematic errors such as those associated with errors in derived  $T_{ex}$ , uncertainties in the  $[C^{18}O/H_2]$  abundance ratio, or errors in the Galactic  $X_{CO}$ .

Downes et al. 1992; Wright et al. 1993). Active star formation is seen only in two of the five central molecular clouds. The molecular cloud densities and temperatures obtained from the CO LVG analysis and HCN emission do not differ by more than a factor of  $\sim 2$  across the five GMCs, but the star formation varies substantially (§ 3.2.3; Downes et al. 1992). The locations of star formation appear to be determined predominantly by dynamics. The two major sites of star formation are located roughly perpendicular to the major axis of the small-scale NIR bar, at the intersection with the spiral arms. This orientation suggests that these star formation sites are at the intersection of the so-called  $x_1$  and  $x_2$  orbits (e.g., Roberts et al. 1979; Athanassoula 1992; Heller & Shlosman 1996).

From CO band head spectroscopy, Böker et al. (1997, 1999) find that the age of the central cluster located in the central trough (not to be confused with the starburst) to be  $10^{6.8-7.8}$  yr old. Based on chemical enrichment models, similar ages are required to explain the anomalous  $C^{18}O$  abundances we find in this region (Henkel & Mauersberger 1993). However, the sites of current star formation (GMCs B and C) are probably younger because they are still sites of radio detected H II regions. The high emission measures ( $EM \gtrsim 10^5 \text{ cm}^{-6} \text{ pc}$ ; Turner & Ho 1983) and the large implied number of O stars suggest that the starburst is younger than 10 Myr, perhaps significantly, and hence younger than the central cluster. Star formation along the arms of the minispiral farther away from the nucleus also appears dynamically induced, perhaps by shocks associated with the bar orbits. The star formation along the leading edge of the spiral arms seen in H $\alpha$  emission can be attributed to the arm molecular gas that is currently upstream (TH92). Taking into account the rotation speed of material in the arms, it is estimated that the star formation is as little as 1 Myr “downstream” from the molecular spiral arms (TH92). Therefore, the star formation on the leading edges of the arms is probably quite young as well (and presumably roughly coeval with the starburst). These results provide additional evidence for the following basic scenario for the recent star formation history of IC 342’s nucleus (Böker et al. 1997). Apparently a star formation event  $\sim 10$ – $30$  Myr ago formed the stars in the central cluster/NIR bar. The bar potential drove the remaining molecular gas into the nucleus along the  $x_1$ -orbits traced by the CO arms. The gas then collided with molecular gas on the perpendicular  $x_2$ -orbits, compressing the gas and triggering the younger currently seen starburst. Such dynamically induced star formation may then explain why such high SFEs are seen only in the central two intersection regions and not elsewhere.

## 5. SUMMARY

Aperture synthesis maps of CO(1–0) and (2–1) in the nucleus of IC 342 are presented. This completes an extensive program of mapping the  $J = 2-1$  and  $J = 1-0$  transitions of CO and its isotopomers. The  $H_2$  column density as traced by optically thin  $C^{18}O$  is similar in morphology to what is implied from  $^{12}CO$  observations, except for two main differences. First, the arms of the nuclear minispiral seen in  $C^{18}O$  (and  $^{13}CO$ ) emission are more symmetric than those seen for  $^{12}CO$ . Isotopic observations demonstrate that the asymmetry in brightness of the  $^{12}CO$  arms are not caused by large differences in the amount of molecular gas

but instead because of asymmetries in optically thick  $^{12}CO$  emissivity. The northern arm is viewed with the starburst “lit” face toward us, appearing brighter in optically thick  $^{12}CO$ , while the southern arm is viewed from the back, with the illuminated side away from the observer.

Second,  $C^{18}O$  is weaker than expected from the  $^{12}CO$  maps across the starburst region. If  $C^{18}O$  accurately traces the amount of molecular gas present, the standard conversion factor from  $^{12}CO$  to  $H_2$ ,  $X_{CO}$ , must be lower than the Galactic value. Comparisons between the column density measured from  $C^{18}O$ , from 1.3 mm dust continuum emission, and from the virial theorem imply that  $X_{CO}(IC\ 342)$  is about  $\frac{1}{2}$  to  $\frac{1}{3}$ . The Galactic  $X_{CO}$  overestimates the amount of  $H_2$  gas in IC 342. For the diffuse gas component at larger distances from the center of IC 342, the conversion factor is about a factor of 2–3 lower still. As a result, a simple scaling of the Galactic conversion factor to an appropriate value for IC 342 is not good enough to characterize the true column density across the starburst.

The mean  $H_2$  column density for the central GMCs is  $\langle N_{H_2} \rangle \simeq 4-5 \times 10^{22} \text{ cm}^{-2}$  ( $A_v \sim 40-50$ ). This corresponds to cloud masses of  $\sim 0.5-1 \times 10^6 M_\odot$ . Excitation temperatures derived from the  $C^{18}O$  data are  $T_{ex} \sim 7-10$  K over much of the central 100 pc. This value is low compared with what is found from the optically thicker  $^{12}CO$  ( $\gtrsim 30$  K) and  $^{13}CO$  (20 K) transitions.  $C^{18}O$  must be subthermally excited over the entire range, indicating that the average densities of the GMCs are not higher than  $n_{crit}(C^{18}O(2-1))$  (or  $\simeq 10^4 \text{ cm}^{-3}$ ). Densities and temperatures obtained for the GMCs from an LVG analysis of  $^{13}CO$  and  $C^{18}O$  are  $\langle n_{H_2} \rangle \simeq 10^{3.5} \text{ cm}^{-3}$  and  $T_{kin} \simeq 10-40$  K. Average densities estimated from the total column densities are consistent with these values. These values are high relative to Galactic disk GMCs but low compared to what is seen in other nearby starburst galaxies (e.g., Jackson et al. 1995).

Our new results indicate that star formation efficiencies are extremely high at the starburst, with  $M_*/M_{gas} \sim 2$  over the central  $\sim 45$  pc. These measurements also indicate that molecular mass fractions in the center of IC 342 are lower than previously estimated, with  $M_{gas}/M_{dyn} \sim 10\%$  for the inner 90 pc rising to  $\sim 30\%$  over the central  $\sim 50$  pc. The locations of star formation in the central  $\sim 200$  pc of IC 342 appear to be determined by large-scale dynamical forces rather than gas surface density. Star formation occurs primarily at the ends of the minispiral arms, oriented perpendicular to the large-scale “bar.” This may be the location of the  $x_1$ - $x_2$  orbit crossings. Weaker star formation is seen downstream of the spiral arms apparently triggered by their passage.

Very low  $^{12}CO(1-0)/C^{18}O(1-0)$  and  $^{13}CO(1-0)/C^{18}O(1-0)$  line ratios seen toward the optically thin central trough region provide evidence that the  $C^{18}O$  abundance is enhanced because of ejecta from the massive stars of the central starburst.

We are grateful to John Carpenter, Dave Frayer, Charlie Qi, Steve Scott, and Dave Woody for their support and assistance in making the observations at OVRO. We also thank Mike Jura for reading the manuscript before submission. We thank the referee for comments that improved the paper. This work was supported in part by NSF grant AST-0071276. The Owens Valley Millimeter Interferometer is operated by Caltech with the support from the NSF.

## REFERENCES

- Aalto, S., Radford, S. J. E., Scoville, N. Z., & Sargent, A. I. 1997, *ApJ*, 475, L107
- Athanassoula, E. 1992, *MNRAS*, 259, 328
- Beck, S. C., Turner, J. L., Ho, P. T. P., Lacy, J. H., & Kelly, D. M. 1996, *ApJ*, 457, 610
- Beck, S. C., Turner, J. L., & Kovo, O. 2000, *AJ*, 120, 244
- Becklin, E. E., Gatley, I., Mathews, K., Neugebauer, G., Sellgren, K., Werner, M. K., & Wynn-Williams, C. G. 1980, *ApJ*, 236, 441
- Böker, T., Förster-Schreiber, N. M., & Genzel, R. 1997, *AJ*, 114, 1883
- Böker, T., van der Marel, R. P., & Vacca, W. D. 1999, *AJ*, 118, 831
- Braine, J., & Combes, F. 1992, *A&A*, 264, 433
- Braine, J., Guélin, M., Dumke, M., Brouillet, N., Herpin, F., & Wielebinski, R. 1997, *A&A*, 326, 963
- Buta, R. J., & McCall, M. L. 1999, *ApJS*, 124, 33
- Cernicharo, J., Bachiller, R., & Duvert, G. 1985, *A&A*, 149, 273
- Crosthwaite, L. P., Turner, J. L., & Ho, P. T. P. 2000, *AJ*, 119, 1720
- Dahmen, G., Hüttemeister, S., Wilson, T. L., & Mauersberger, R. 1998, *A&A*, 331, 959
- De Jong, T., Chu, S.-I., & Dalgarno, A. 1975, *ApJ*, 199, 69
- de Vaucouleurs, G., de Vaucouleurs, A., & Corwin, H. G. 1976, *Second Reference Catalog of Bright Galaxies* (Austin: Univ. Texas Press)
- Downes, D., Radford, S. J. E., Giulloteau, S., Guélin, M., Greve, A., & Morris, D. 1992, *A&A*, 262, 424
- Eckart, A., Downes, D., Genzel, R., Harris, A. I., Jaffe, D. T., & Wild, W. 1990, *ApJ*, 348, 434
- Elmegreen, B. G. 1989, *ApJ*, 338, 178
- Frerking, M. A., Langer, W. D., & Wilson, R. W. 1982, *ApJ*, 262, 590
- Goldreich, P., & Kwan, J. 1974, *ApJ*, 189, 441
- Goldsmith, P. F., Bergin, E. A., & Lis, D. C. 1997, *ApJ*, 491, 615
- Gordon, M. A., Berkemann, U., Mezger, P. G., Zylka, R., Haslam, C. G. T., Kreysa, E., Sievers, A., & Lemke, R. 1993, *A&A*, 280, 208
- Heller, C. H., & Shlosman, I. 1996, *ApJ*, 471, 143
- Henkel, C., Chin, Y.-N., Mauersberger, R., & Whiteoak, J. B. 1998, *A&A*, 329, 443
- Henkel, C., & Mauersberger, R. 1993, *A&A*, 274, 730
- Henkel, C., Wilson, T. L., Langer, N., Chin, Y.-N., & Mauersberger, R. 1994, *The Structure and Content of Molecular Clouds*, ed. T. L. Wilson & K. J. Johnston (Berlin: Springer), 72
- Hildebrand, R. H. 1983, *QJRAS*, 24, 267
- Hunter, S. D., et al. 1997, *ApJ*, 481, 205
- Hurt, R. L., & Turner, J. L. 1991, *ApJ*, 377, 434
- Hüttemeister, S., Wilson, T. L., Mauersberger, R., Lemme, C., Dahmen, G., & Henkel, C. 1995, *A&A*, 294, 667
- Ishizuki, S., Kawabe, R., Ishiguro, M., Okumura, S. K., Morita, K.-I., Chikada, Y., & Kasuga, T. 1990, *Nature*, 344, 224
- Jackson, J. M., Paglione, T. A., Carlstrom, J. E., & Rieu, Nguyen-Q. 1995, *ApJ*, 438, 695
- Karachentsev, I. D., & Tikhonov, N. A. 1993, *A&AS*, 100, 227
- Langer, W. D., Goldsmith, P. F., Carlson, E. R., & Wilson, R. W. 1980, *ApJ*, 235, L39
- Langer, W. D., Graedel, T. E., Frerking, M. A., & Armentrout, P. B. 1984, *ApJ*, 277, 581
- Levine, D., Turner, J. L., & Hurt, R. L. 1994, in *IAU Colloq. 140, Astronomy with Millimeter and Submillimeter Wave Interferometry*, ed. M. Ishiguro & W. J. Welch (San Francisco: ASP), 339
- Lo, K. Y., et al. 1984, *ApJ*, 282, L59
- MacLaren, I., Richardson, K. M., & Wolfendale, A. W. 1988, *ApJ*, 333, 821
- Madore, B. F., & Freedman, W. L. 1992, *PASP*, 104, 362
- Maloney, P., & Black, J. H. 1988, *ApJ*, 325, 389
- Matsushita, S., Kohno, K., Vila-Vilaro, B., Tosaki, T., & Kawabe, R. 1998, *ApJ*, 495, 267
- Mauersberger, R., Henkel, C., Whiteoak, J. B., Chin, Y.-N., & Tieftrunk, A. R. 1996, *A&A*, 306, 141
- McCall, M. L. 1989, *AJ*, 97, 1341
- Meier, D. S., Turner, J. L., & Hurt, R. L. 2000, *ApJ*, 531, 200 (MTH00)
- Mezger, P. G., & Henderson, A. P. 1967, *ApJ*, 147, 471
- Nakai, N., & Kuno, N. 1995, *PASJ*, 47, 761
- Neininger, N., Guélin, M., Klein, U., Garcia-Burillo, S., & Wielebinski, R. 1998, *A&A*, 339, 737
- Oka, T., Hasegawa, T., Sato, F., Tsuboi, M., & Miyazaki, A. 1998, *ApJS*, 118, 455
- Padin, S., Scott, S. L., Woody, D. P., Scoville, N. Z., Seling, T. V., Finch, R. P., Ciovanine, C. J., & Lowrance, R. P. 1991, *PASP*, 103, 461
- Papadopoulos, P. P., Seaquist, E. R., & Scoville, N. Z. 1996, *ApJ*, 465, 173
- Pollack, J. B., Hollenbach, D., Beckwith, S., Simonelli, D. P., Roush, T., & Fong, W. 1994, *ApJ*, 421, 615
- Prantzos, N., Aubert, O., & Audouze, J. 1996, *A&A*, 309, 760
- Reynaud, D., & Downes, D. 1999, *A&A*, 347, 37
- Rickard, L. J., & Harvey, P. M. 1984, *AJ*, 89, 1520
- Roberts, W. W., Huntley, J. M., & van Albada, G. D. 1979, *ApJ*, 233, 67
- Sakamoto, S. 1996, *ApJ*, 462, 215
- Scoville, N. Z., Carlstrom, J., Padin, S., Sargent, A., Scott, S., & Woody, D. 1994, in *IAU Colloq. 140, Astronomy with Millimeter and Submillimeter Wave Interferometry*, ed. M. Ishiguro & J. Welch (San Francisco: ASP), 10
- Scoville, N. Z., & Sanders, D. B. 1987, *Interstellar Processes*, ed. D. J. Hollenbach & H. A. Thronson (Dordrecht: Kluwer), 21
- Scoville, N. Z., & Solomon, P. M. 1974, *ApJ*, 187, L67
- Scoville, N. Z., Yun, M. S., Clemens, D. P., Sanders, D. B., & Waller, W. H. 1987, *ApJS*, 63, 821
- Smith, P. A., Brand, P. W. J. L., Mountain, C. M., Puxley, P. J., & Nakai, N. 1991, *MNRAS*, 252, 6
- Sodroski, T. J., et al. 1994, *ApJ*, 428, 638
- Solomon, P. M., Rivolo, A. R., Barrett, J. W., & Yahil, A. 1987, *ApJ*, 319, 730
- Strong, A. W., et al. 1988, *A&A*, 207, 1
- Turner, J. L., & Ho, P. T. P. 1983, *ApJ*, 268, L79
- Turner, J. L., Ho, P. T. P., & Beck, S. C. 1998, *AJ*, 116, 1212
- Turner, J. L., & Hurt, R. L. 1992, *ApJ*, 384, 72 (TH92)
- Turner, J. L., Hurt, R. L., & Hudson, D. Y. 1993, *ApJ*, 413, L19
- Vacca, W. D., Garmany, C. C., & Shull, J. M. 1996, *ApJ*, 460, 914
- van Dishoeck, E. F., & Black, J. H. 1988, *ApJ*, 334, 771
- Wall, W. F., & Jaffe, D. T. 1990, *ApJ*, 361, L45
- Wilson, T. L., & Matteucci, F. 1992, *A&A Rev.*, 4, 1
- Wilson, C. D., & Scoville, N. Z. 1990, *ApJ*, 363, 435
- Wilson, T. L., & Rood, R. 1994, *ARA&A*, 32, 191
- Wright, M. C. H., Ishizuki, S., Turner, J. L., Ho, P. T. P., & Lo, K. Y. 1993, *ApJ*, 406, 470
- Xie, S., Young, J., & Schloerb, F. P. 1994, *ApJ*, 421, 434